Porphyrin-Containing MOFs and COFs as Heterogeneous Photosensitizers for Singlet Oxygen-Based Antimicrobial Nanodevices

Adrien Schlachter, Paul Asselin, Pierre Harvey

Porphyrin-containing MOFs and COFs as Heterogeneous Photosensitizers for Singlet Oxygen-based Antimicrobial Nanodevices

*Adrien Schlachter, Paul Asselin and Pierre D. Harvey**

Département de chimie, Université de Sherbrooke, Sherbrooke, PQ, Canada, J1K 2R1.

*Corresponding author. E-mail address: Pierre.Harvey@USherbrooke.ca (P.D. Harvey)

KEYWORDS: Metal organic frameworks, Covalent organic frameworks, Singlet oxygen, Antimicrobial agents, Nanomaterials, Antibacterial photodynamic therapy.

ABSTRACT: Visible light irradiation of porphyrin and metalloporphyrin dyes in the presence of molecular oxygen can result in the photo-catalytic generation of singlet oxygen ($^1O_2$). This type II reactive oxygen species (ROS) finds many applications where the dye, also called photosensitizer, is dissolved (*i.e.* homogeneous phase) along with the substrate to be oxidized. In contrast, metal-organic frameworks (MOFs) are insoluble (or will disassemble) when placed in a solvent. When stable as a suspension, MOFs adsorb a large amount of O_2 and photo-catalytically generate $^1O_2$ in a *heterogeneous* process efficiently. Considering the immense surface area and great capacity for gas adsorption of MOFs, they seem ideal candidates for this application. Very recently, covalent-organic frameworks (COFs), variants where reticulation relies on covalent rather than coordination bonds, have emerged as efficient photosensitizers. This comprehensive mini review describes recent developments in the use of porphyrin-based or porphyrin-containing MOFs and COFs, including nanosized versions, as heterogeneous photosensitizers of singlet oxygen towards antimicrobial applications.

CONTENTS

1. Introduction

Originally of great interest for astrophysical sciences, singlet oxygen, $^1O_2$ ($^1\Delta_g$), was first observed by the Nobel laureate G. Herzberg in 1934.[1] Since this discovery, the notorious reactivity of this species was recognized throughout the world [2] and led to an important medicinal application: photodynamic therapy, PDT, well demonstrated by various porphyrin dyes and metalloporphyrin derivatives.[3] Over the past five years, this porphyrin-driven PDT strategy has been extended to metal-organic frameworks, MOFs, which has very recently been reviewed.[4] Concurrently, MOFs constructed with porphyrin and metalloporphyrin multidentate units have also received quite a bit of attention for photo-induced CO_2 reduction, O_2 and H_2 evolution, oxidation of organics including pollutants, reduction of inorganics, and antibacterial properties. A few of these topics have also been recently reviewed.[5–11] Similarly, porphyrin-based COFs are also known to exhibit photocatalytic properties,[8] including efficient photoinduced generation of $^1O_2(^1\Delta_g)$ as their applications in photodynamic therapy are also well-established.[3] The porous nano-MOFs and nano-COFs generally have a very large surface area thus permitting a larger production of $^1O_2(^1\Delta_g)$. This ROS reacts with the cell walls of bacteria breaking chemical bonds leading to the

collapse of the walls and cell death. The area of heterogeneous photocatalysts for singlet oxygen-based processes and applications using porphyrin and metalloporphyrin-containing MOFs and COFs has experienced a booming interest over the past three years (**Figure 1**).

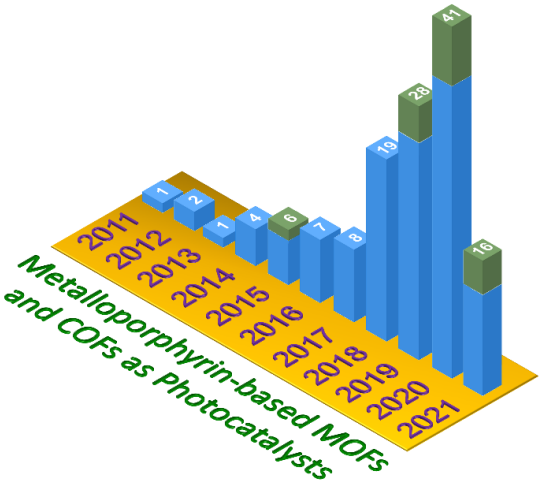

Figure 1. Number of research reports on porphyrin-containing MOFs (blue) and COFs (green), along with their corresponding nanosized versions, used as photocatalysts. These data exclude reports related to photodynamic therapy of cancer cells.

Recent studies focused on using MOF and COF as photosensitizers for antimicrobial applications. This endeavour is readily motivated by the recurrent and stubborn resistance of bacteria towards current antibiotics, often due to abuse, that makes bacterial infections a serious problem. Indeed, when one considers that there are 17 million infected people annually,[12] and that many people die due to drug resistant bacteria,[13] bacterial infection is a particularly important health issue that imposes a large financial burden to society. It is noteworthy that several porphyrin-based MOFs and COFs have demonstrated a better ability to generate $^1O_2(^1\Delta_g)$ than porphyrins and metalloporphyrins alone.[14] This is indeed the case for the MOF commonly labelled PCN-224 in which Zr_6 clusters ($Zr_6(\mu_3\text{-}O)_4(\mu_3\text{-}OH)_4(OH)_6(H_2O)_6(COO)_6$) are used as nodes and the porphyrin photosensitizers are tetrakis(carboxyphenyl)porphyrin ($TCPP^{4-}$, see **Figure 2** for structure), which is widely used in antibacterial photodynamic therapy. This comprehensive minireview summarizes the recent developments of the porphyrin-containing MOFs and COFs and corresponding nanosized versions used as photosensitizers for antibacterial properties. It is noteworthy that COFs are recently discovered materials and the field is yet to be developed. Because of their structural similarity with MOFs, they are included in this review.

2. Ground and excited states of molecular oxygen

Molecular oxygen's exhibits the ground state electronic configuration $(\sigma_s)^2(\sigma_s^*)^2(\sigma_p)^2(\pi)^4(\pi^*)^2(\sigma_p^*)^0$. The π^* manifolds degeneracy leads to three distinct electronic states: a ground state ($^3\Sigma_g^-$), and two excited states ($^1\Delta_g$ and $^1\Sigma_g^+$). The relative energies separating the ground from the excited states are 0.9773 and 1.6268 eV for $^1\Delta_g$ and $^1\Sigma_g^+$, respectively.[15] Below are the common methods used to generate singlet oxygen, direct and indirect detection of singlet oxygen using MOFs.

2.1. Common methods to generate singlet oxygen

The direct light excitation of molecular oxygen ($O_2(^3\Sigma_g^-) + h\nu \rightarrow O_2(^1\Delta_g)$) is inefficient due to the strongly forbidden nature of this electric dipole in the electronic transition. Instead, two major routes are generally used: bimolecular energy transfer using a sensitizer (dye*; in either singlet or triplet excited states), and electrochemistry. Energy transfer from a sensitizer to O_2 is an efficient collisional process (**equation 1**), which is thermodynamically downhill (**Figure 2**).

$$\text{dye}^* + O_2\,(^3\Sigma_g^-) \rightarrow \text{dye} + O_2\,(^1\Delta_g) + \text{heat} \qquad \textbf{(1)}$$

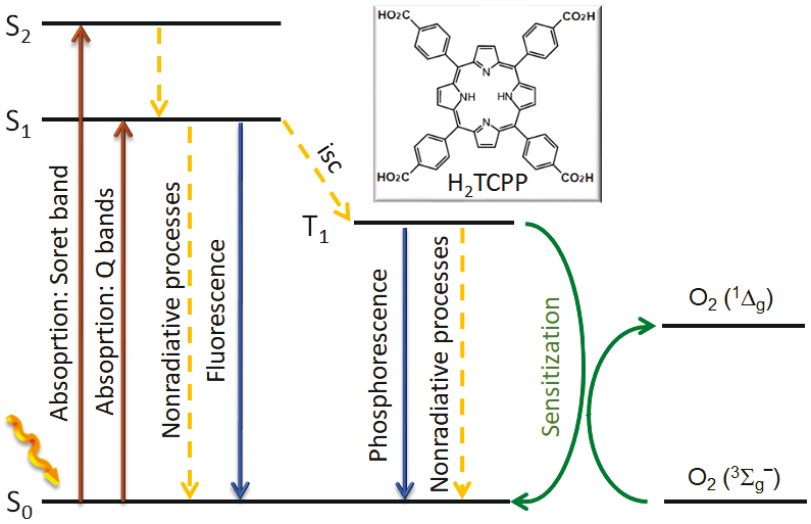

Figure 2. State diagram showing the photophysical events processes for porphyrin species after absorption of light (isc = intersystem crossing), and the sensitization process with molecular oxygen. Note that sensitization from the S_1 state is possible but less probable as its lifetime is short.

The collisional mechanism by which photosensitization occurs has been demonstrated using various cofacial bis(metalloporphyrin)s separated rigid spacers, thus blocking access one side of

the excited porphyrins to molecular oxygen.[16] This antenna effect results in a quenching of the excited states of the dye* undergoing energy transfer thus decreasing the singlet and triplet lifetimes as well as their corresponding emission intensities.[16,17] Generally, triplet excited states are more prone to sensitization because of their longer lifetimes. Sensitization of molecular oxygen by MOFs built with porphyrin and metalloporphyrin ligands is also well documented.[18–20]

Electrochemical formation of singlet oxygen proceeds through the reduction of molecular oxygen from an electrochemically reduced mediator MOF at the anode. This generated intermediate is the superoxide $O_2^{\bullet -}$, a ROS. The latter species can be re-oxidized at the cathode, to produce singlet oxygen. The overall processes (simplified as: O_2 ($^3\Sigma_g^-$) + electric energy → O_2 ($^1\Delta_g$)) are indicated in **equations 2-4**:

$$MOF + 1\ e^- \rightarrow [MOF]^{\bullet -} \quad \text{(anode)} \qquad (2)$$

$$[MOF]^{\bullet -} + O_2\ (^3\Sigma_g^-) \rightarrow O_2^{\bullet -} + MOF \qquad (3)$$

$$O_2^{\bullet -} \rightarrow O_2\ (^1\Delta_g) + 1\ e^- \quad \text{(cathode)} \qquad (4)$$

Recent examples include Zr-based metal–organic framework with zinc tetrakis(carboxyphenyl)-porphyrin (ZnTCPP) groups (MOF-525-Zn).[21,22]

2.2. Direct detection of singlet oxygen

The direct detection of $O_2(^1\Delta_g)$ in the gas phase can be performed using electron paramagnetic resonance, EPR, spectroscopy.[23] While $O_2(^3\Sigma_g^-)$ is paramagnetic and thus is EPR active, $O_2(^1\Delta_g)$ is diamagnetic but is still EPR active because of its net electron orbital angular momentum of J = 2 giving rise to four EPR transitions (J = -2 → J = -1, J = -1 → J = 0, J = 0 → J = 1, and J = 1 → J = 2). According to Fermi-Wentzel's golden rule, of relative amplitudes of 2.00, 2.45, 2.45 and 2.00, respectively.[24] One recent example of such gas phase measurements was reported by N. J. Turro and his collaborators (**Figure 3**, left).[25] $O_2(^1\Delta_g)$ can be directly generated by a microwave discharge ($O_2(^3\Sigma_g^-)$ + energy → $O_2(^1\Delta_g)$) or sensitized (equation 1) by naphthalene in a O_2(g) flow. This spectrum is used as a fingerprint for the direct confirmation of the presence of $O_2(^1\Delta_g)$ in the medium. However, pulsed techniques are necessary for the detection of this intermediate, which are often generated in small amount. In Turro's work, the reported lifetime (τ) is 0.4 s, for a pressure of 0.4 Torr,[25] but a longer lifetime (7 s) has also been reported.[26] Interestingly, the

radiative lifetime of $O_2(^1\Delta_g)$ has been calculated to be 45 mins for a pressure of 0 torr.[27] Because of this relative short lifetime in ordinary conditions, combined with the small amount of generated $O_2(^1\Delta_g)$, spin-trapping of this highly reactive intermediate is a far more convenient technical approach (described below). To the best of our knowledge, there seems to be no direct EPR observation of $O_2(^1\Delta_g)$ when generated by porphyrin-MOF sensitization.

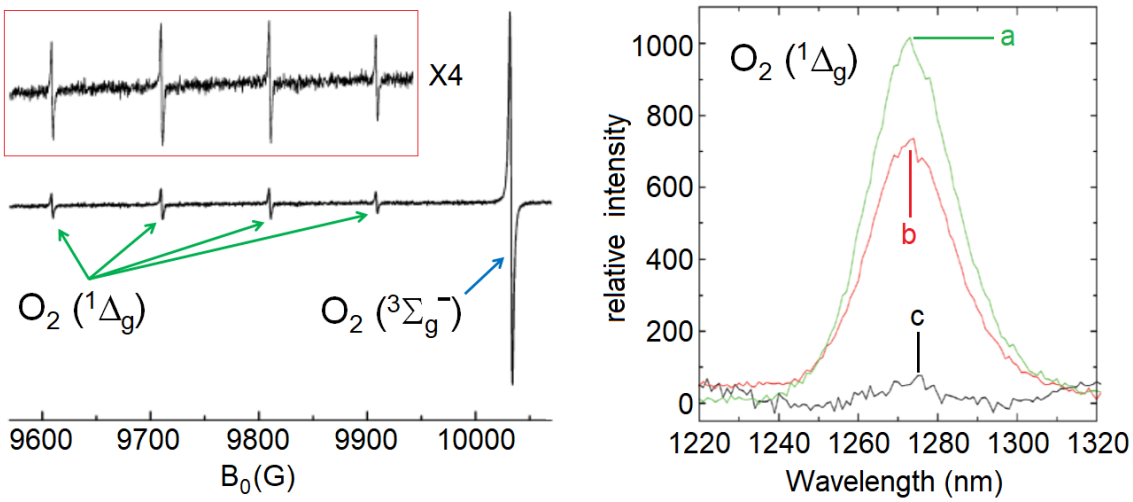

Figure 3. Left: EPR spectra of $O_2(^1\Delta_g)$ at 293 K generated by microwave discharge (P = 0.2 Torr). Reproduced from ref 25 with permission. Copyright 2013 American Chemical Society. Right: Phosphorescence spectra of photosensitized $O_2(^1\Delta_g)$ produced in acetonitrile dispersions of the network 3D-PdTPP (*i.e.* COF) saturated with O_2 (a), air (b), and Ar atmosphere (c) upon excitation at 420 nm. Reproduced from ref 28 with permission. Copyright 2016 Royal Society of Chemistry.

Conversely, the direct detection of $O_2(^1\Delta_g)$ is performed by emission spectroscopy (λ_{emi} = 1268-1275 nm), regardless of the method used to generate it (*i.e.* chemi-, electrochemi-, or photoluminescence).[2] A typical example is shown in **Figure 3** (right) where $O_2(^1\Delta_g)$ is produced from sensitization with the network 3D-PdTPP constructed with the tetrakis(4-phenylboronic acid) linker and (5,10,15,20-tetrakis(4-bromophenyl)porphyrinpalladium(II) as sensitizer.[28] The 3D-COF is suspended in an organic solvent containing dissolved molecular oxygen. Then, a heterogeneous sensitization process (solid-liquid) takes place. The phosphorescence lifetime, τ_P, of $O_2(^1\Delta_g)$ is significantly affected by the environment. In the gas phase the excited molecule persists for 10^{-3}-10^0 s. This duration is cut short by several orders of magnitude depending on whether $O_2(^1\Delta_g)$ exists in solution or inside a porous MOFs. For instance, the τ_P value for $O_2(^1\Delta_g)$

generated inside the pores of a MOF built upon 5,10,15,20-tetrakis(4-sulfonatophenyl)porphyrin and oxometalate cluster $[Eu_6(\mu_6\text{-}O)(\mu_3\text{-}OH)_8(H_2O)_{14}]^{8+}$ is 21 ± 1 μs.[18]

Chemical generation of singlet oxygen can also be performed. The most common method involves the use of peroxides (for example $H_2O_2 + {}^{-}OCl \rightarrow O_2(^1\Delta_g) + H_2O + Cl^-$).[29] Chemically generated $O_2(^1\Delta_g)$ has the particularity that the amount can be significantly larger than the direct excitation method or the sensitization process since the quantity of reactants can intrinsically be larger. This situation has a parallel outcome as $O_2(^1\Delta_g)$ can dimerize to form $(^1O_2)_2$; a ROS that is reminiscent of an excimer ($O_2(^1\Delta_g) + O_2(^1\Delta_g) \rightarrow (^1O_2)_2$).[29] Upon relaxation, two equivalents of $O_2(^3\Sigma_g^-)$ are reformed along with the production of an emission, hν, at 633 nm: $(^1O_2)_2 \rightarrow 2\ O_2(^3\Sigma_g^-) + h\nu$. The combination of the excited state energy for two equivalents of $O_2(^1\Delta_g)$ (15764.8 cm^{-1} or 1.9546 eV) corresponds to the emission energy of the $(^1O_2)_2$ dimer (633 nm, 15798 cm^{-1}).

However, in the context of porphyrin dyes and porphyrin-containing MOFs, one major drawback of this photosensitizer approach is the high reactivity of type I ROS toward these pigments and ligands when used in large quantity,[30] or upon a prolonged period of irradiation in the presence of dissolved O_2.[31] Significant stability problems may occur as the dye undergoes bleaching at the hands of the very ROS it generates. Alternatively, devices electrogenerating chemiluminescence of $O_2(^1\Delta_g)$, or more accurately $(^1O_2)_2$, using porphyrin-containing MOFs,[21,22] and materials, have been designed.[32,33] In these cases, the characteristic electrochemiluminescence produces the characteristic emission at 633 nm thus witnessing the presence $O_2(^1\Delta_g)$ within the devices.

2.3. Indirect detection of singlet oxygen

The three main methods to indirectly detect $O_2(^1\Delta_g)$ are the use of the spin-traps (and EPR spectroscopy), observation of quenching of the porphyrin singlet and triplet emissions (upon saturating the solution with O_2 *vs.* Ar), and the monitoring of the photo-induced degradation of a known dye, which can provide information on the quantum yield of $O_2(^1\Delta_g)$ generation. Other techniques such as time-resolved thermal lensing,[34] sono-photochemistry,[35] and photocalorimetry [36] are also known but are not extensively used.

A representative example for the use of spin-trapping and emission quenching by $O_2(^1\Delta_g)$ is presented in **Figure 4.**[37] In this example, tetrakis(carbonyl phenyl)porphyrinpalladium(II), Pd-TCPP, is mixed with dodecyl-α,ω-bis (N,N-dimethyl-N-dodecylammonium) bromide and N,N′-

dibenzoyl-L-cystine, which together form micelle-hybridized supramolecular gels, called M/DBC gels. Upon irradiation at 418 nm (*i.e.* in the Soret band of Pd-TCPP), $O_2(^1\Delta_g)$ is generated by sensitization and can be trapped by 2,2,6,6-tetramethylpiperidine (TEMP) to form the stable radical TEMPO (2,2,6,6-tetramethylpiperidin-1-yl)oxyl) according to Scheme 1. The latter species is EPR-active and exhibits a triplet signal of equal intensity (**Figure 4**, left). This method is the most frequently used technique throughout the literature to unambiguously demonstrate the presence of $O_2(^1\Delta_g)$ in the medium. Concurrently, the removal of oxygen (in this case, it consists in irradiating in the UV region to activate the S-S bond in N,N′-dibenzoyl-L-cystine, which then react with O_2) provides a higher intensity signal from the Pd-TCPP emission. The quenching of the porphyrin emission by oxygen is accompanied by a decrease in emission intensity proportional to the quantity of quencher (*i.e.* Stern-Volmer approach). Experience shows that three conditions are generally used for such study (inert atmosphere, in air, in pure O_2) as shown in **Figure 3**, right.

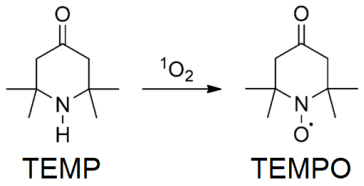

Scheme 1. Oxidation of TEMP by $O_2(^1\Delta_g)$.

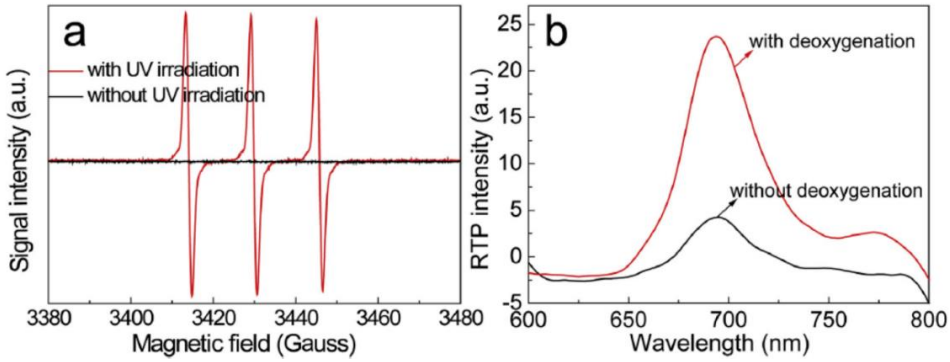

Figure 4. (a) EPR spectrum of a Pd-TCPP inside a M/DBC gel in the presence (thus generating $O_2(^1\Delta_g)$) and the absence of UV irradiation. (b) Phosphorescence spectrum of Pd-TCPP in a M/DBC gel with and without deoxygenation (*i.e.* respectively without and with molecular oxygen,). Reproduced from ref 37 with permission. Copyright 2019 Elsevier.

The third indirect method involves the use of oxygen traps and permits the measurement of the singlet oxygen quantum yields, $\Phi(^1O_2)$ in some cases.[38–41] Several examples of oxygen traps are

shown in **Figure 5** and their reactivity towards $O_2(^1\Delta_g)$ can be monitored by UV-vis (similar to actinometry) or fluorescence spectroscopy, and more rarely, by the change in gas pressure. One of the oldest types of spin traps are 9,10-disubstituted anthracene derivatives and their reactivity towards $O_2(^1\Delta_g)$ is represented in **Scheme 2a**.[42] A recent example is the 2D-MOF formulated as [Tb(μ_2-OH)(TCPP)$_{0.5}$] (Tb-TCPP), which is used as a sensitizer.[43] The presence of $O_2(^1\Delta_g)$ is demonstrated by its reactivity towards 9,10-diphenyl anthracene disrupting its absorption or fluorescence bands. Nowadays, the fluorescent 1,3-diphenylisobenzofuran (DPBF) is the most common oxygen trap, which also exhibits a particularly specific reactivity towards $O_2(^1\Delta_g)$. It forms an endoperoxide upon reacting with $O_2(^1\Delta_g)$ and transforms in the diketone 1,2-dibenzoylbenzene (**Scheme 2b**). The reaction between $O_2(^1\Delta_g)$ and DPBF is generally spectroscopically monitored where its fluorescence intensity is recorded as a function of time. Fluorescence is often preferred to avoid the undesired spectral overlap between the absorbance of the chemical traps and photosensitizer. DPBF is also used as a comparative standard for the measurements of $\Phi(^1O_2)$. A few recent examples using DPBF as an $O_2(^1\Delta_g)$ fluorescent indicator or a tool to evaluate the performance of porphyrin-based MOFs as photosensitizers for the generation of $O_2(^1\Delta_g)$, have indeed been reported.[44–47] An example where absorption spectroscopy (*i.e.* colorimetry) was employed to detect $O_2(^1\Delta_g)$ is presented in **Figure 6**.[48] In this case, nanosheets of a MOF built upon Ni-TCPP and a Zr_6 cluster as a node (UNs-FA), which absorbs in the 300-700 nm region were prepared and characterized. Upon irradiation, the reaction between $O_2(^1\Delta_g)$ and DPBF occurs at the surface of the 2D-MOF catalyst and the conversion of DPBF into the corresponding endoperoxide.

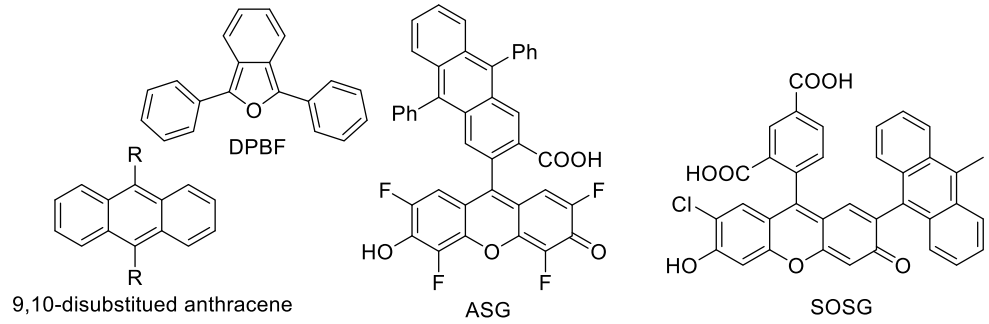

Figure 5. Structure of common molecular traps for $O_2(^1\Delta_g)$. ASG = Aarhus Sensor Green, SOSG = Singlet Oxygen Sensor Green (commercially available).

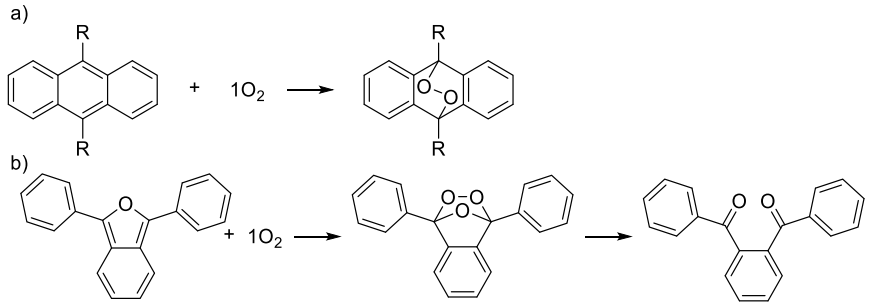

Scheme 2. Reactivity of $O_2(^1\Delta_g)$ towards 9,10-disubstituted anthracenes (a) and DPBF (b).

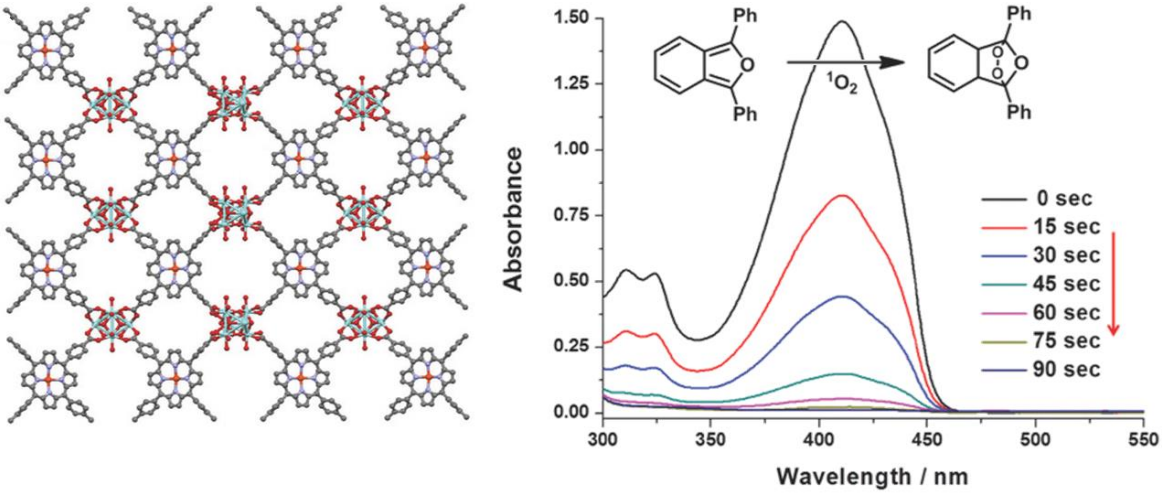

Figure 6. Left: Illustration of the 2D MOF (UNs-FA) containing Ni-TCPP and a Zr_6-cluster. Right: Changes of the absorption spectrum of DPBF upon being exposed to the surface of UNs-FA under irradiation. Reproduced from ref. 48 with permission. Copyright 2018 Wiley-VCH.

3. Antenna effect and semi-conductivity

A required property for photosensitization is the possibility of efficient excitation energy funnelling across the bulk (antenna effect; **Figure 7**). Porphryin-based MOFs have this ability and the energy hopping process is believed to occur *via* a through space dipole-dipole Forster mechanism.[49] This displacement of singlet excitons is typically monitored by fluorescence quenching experiments.[50,51] In these two studies, the extent of the photogenerated exciton went up to ~45 porphyrin units in one case [50] and up to 60 nm in the other,[51] thus illustrating the significant efficiency of the migration of the singlet exciton. This conclusion is consistent with the evaluated time scale for such an energy funnelling (1 ps) in a very recent investigation.[52] Although this was not specifically pointed out in these studies, this efficiency benefits from the short distances between the porphyrin units and the favorable orientation factor of their transition moments, which

are important parameters of the Forster's theory.[53] Concurrently using nanosecond transient absorption spectroscopy, the triplet exciton is found to be somewhat slower (ns) and less delocalized where a distance of 17.3 nm was obtained for the MOF PCN-223.[54] This outcome is consistent with the fact that the J-integral (*i.e.* spectral overlap between the phosphorescence band of the donor with the absorption band of the acceptor) is smaller than that of the singlet one simply because the absorptivity values for the spin-forbidden transitions are significantly smaller than those for the allowed ones. Consequently, the rates of energy migrations in the triplet states are bound to be slower, therefore less extensive.

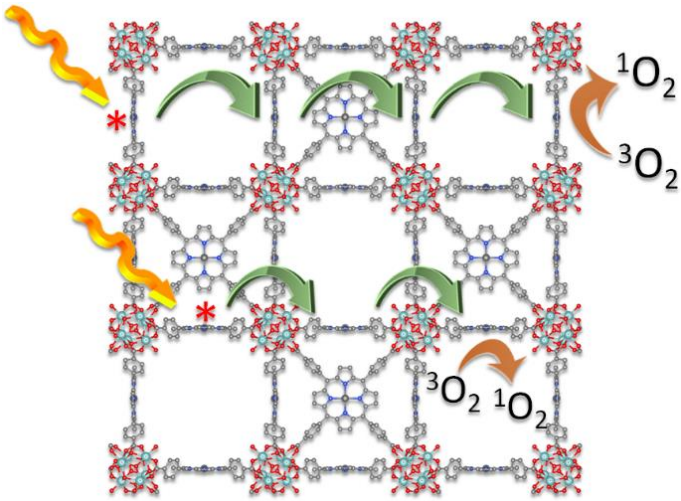

Figure 7. Process of exciton (*) energy migration (green arrows) across a MOF (here PCN-224 as a representative example; the image of the MOF was reproduced using the cif file).

Multiple MOFs have demonstrated semi- and photo-conducting properties even in the absence of doping.[55–59] This feature has been established using exclusively 2D MOFs for technical reasons. This presence of charge or hole carriers within the MOFs, which was briefly alluded to above when mentioning the design of electroluminescent devices, has an important impact on the possible concomitant photo-induced redox processes. In the absence of heterojunction inherent in composite materials (described below), the metallic cluster may occasionally act as a redox partner. In a recent investigation,[60] it was demonstrated that H_2TCPP acted as the electron donor, and the zirconium cluster ($Zr_6(\mu_3\text{-})_4(\mu_3\text{-OH})_4(OH)_4(H_2O)_4(COO)_8$; PCN-222), the electron acceptor. Conversion of $^3O_2$ into $O_2^{\bullet -}$ (called Type I ROS) was demonstrated using superoxide scavengers (isopropyl alcohol and dinitrogen). Other examples exist.[61,62] Concerning COFs, the

absence of a redox partner, conductivity requires doping or the design of an adequate composite material using a semi-conducting material.[63,64] The Type I ROS includes H_2O_2, HO•, and O_2^-.

4. MOF and COF designs, and related properties.

Porphyrins and metalloporphyrins as such are well-known to exhibit photocatalytic antimicrobial properties.[65,66] Their incorporations as building blocks for the preparation of both 2D- and 3D-frameworks are also well-documented and the various synthetic methodologies have recently been thoroughly reviewed (COFs [67,68] and MOFs [69,70]). For instance, the construction of 3D-COFs may proceed upon condensing tetrahedral and quadrilateral building blocks such as a tetrafuntionalized porphyrin unit under solvothermal conditions (**Figure 8**, left), whereas the design of 2D COFs proceeds with a linear building block (**Figure 8**, right). Other binding strategies such as Suzuki and Sonogashira palladium coupling between C-Br and C-Ar and C≡C-H units respectively, exists (**Scheme 3**).[71,72] The large porosity of these 2D- and 3D-materials are evaluated by BET analysis and the propensity to photocatalyze the generation of $O_2(^1\Delta_g)$ is also well demonstrated.[73,74]

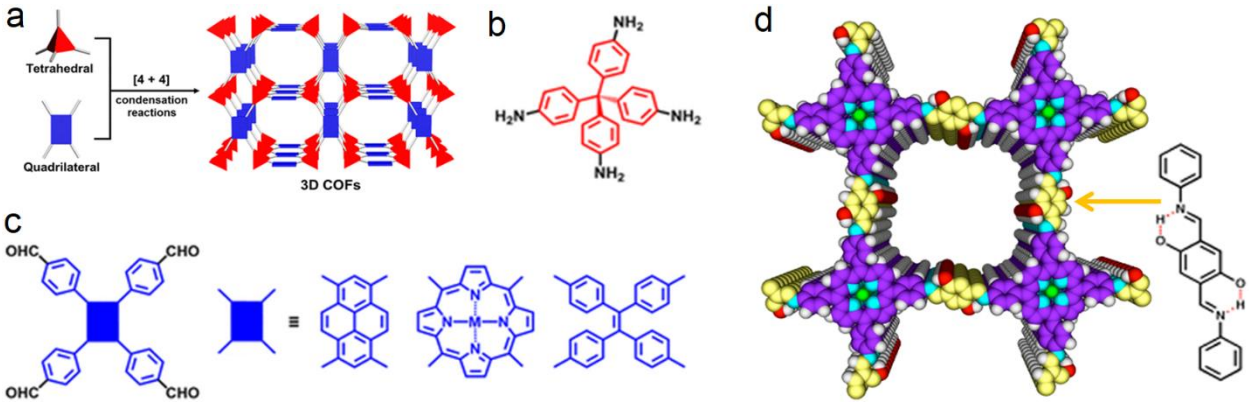

Figure 8. (a) One possible approach for the construction of 3D COFs *via* the [4+4] condensation of tetrahedral and quadrilateral building blocks. (b) Structure of one example of a tetrahedral block (tetra(p-aminophenyl)methane). (c) Three examples of motif of quadrilateral building blocks: from left to right, 1,3,6,8-tetrakis(4-formylphenyl)pyrene, 5,10,15,20-tetra(4-benzaldehyde)porphyrin (metallated or free base), and ethylenetetra(4-benzaldehyde). Reproduced from ref 68 with permission. Copyright 2020 American Chemical Society. (d) Example of a 2D COF using 5,10,15,20-tetra(4-phenylamino)porphyrin(metal(II)) (M = 2H, Cu, Pd) and dihydroxyterephthalaldehyde as starting materials. The spacer-to-spacer distance is 2.5 nm. Reproduced from ref 73 with permission. Copyright 2020 American Society.

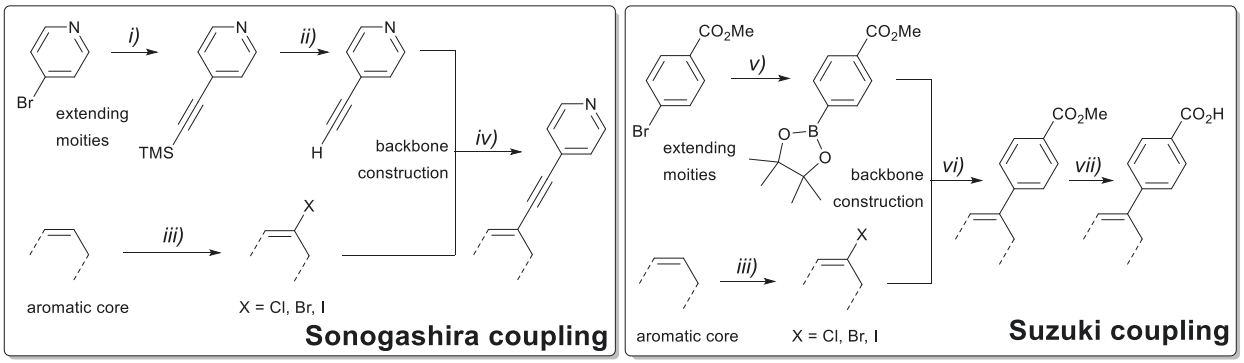

Scheme 3. Example of construction and extension of organic linker backbone for two types of binding groupments. Left, *via* Sonogashira coupling and right, *via* Suzuki coupling. *i*) C≡CTMS, Pd(II) catalyst , Cu(I) cocatalyst *ii*) TBAF, *iii*) NIS or NBS or NCS *iv*) Pd(0) catalyst, Cu(I) cocatalyst ; *v*) bimolecular dioxaborolane, AcOK, Pd(II) catalyst ; *vi*) Pd(0) catalyst ; *vii*) KOH.

Examples of 3D MOFs issued from a solvothermal reaction between TCPP and a zirconium salt, often $ZrOCl_2$ or $ZrCl_4$, may lead to different structures where the resulting zirconium cluster has the general formula $Zr_6(\mu_3\text{-}O)_4(\mu_3\text{-}OH)_4(OH)_{12\text{-}n}(H_2O)_{12\text{-}n}(COO)_n$ (n = 6 (PCN-224), 8 (PCN-222) and 12 (PCN-223; **Figure 9**).[75] An example of a 2D MOF is provided in **Figure 6**. Construction of composites comprising of, for instance, gold nanorods, polydopamine nanoparticles (NPs), and polydopamine/platinum nanoparticles inside the pores of the MOFs or deposited onto graphene oxide does not preclude the photosensitization of $O_2(^1\Delta_g)$.[76] A large effort has been made to render MOFs biocompatible with post-surface functionalization (for example, folic acid and lactic-*co*-glycolic acid), both inside and outside the MOF scaffolding, composite fabrication (including the use of nano-particles) thus permitting applications in bioactive molecules and advance drug delivery, and when processed as thin films, also having antimicrobial properties.[77]

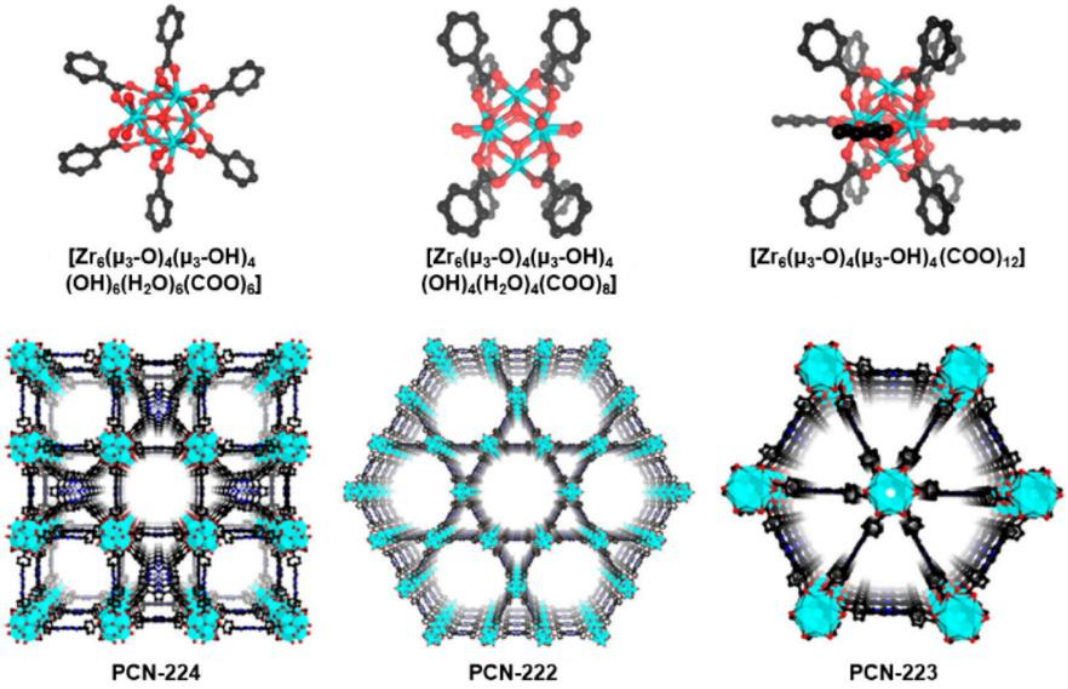

Figure 9. Structures of MOFs issued from the reactions between TCPP and zirconium salts. Reproduced from ref 75 with permission. Copyright 2020 Elsevier.

An interesting hybrid between of 2D MOF and COF has also been reported as an intermediate 2D material between a 2D MOF (called SURMOF) and a 2D COF (called SURGEL; **Figure 10**).[78] The approach involves a porphyrin core (in this example a free base) functionalized by two carboxylate groups (susceptible to react with zinc salt), and by two azide units (therefore susceptible to react with ethynyl function via click chemistry). The first step consists of forming a 2D MOF, which pre-programs the positions of the azide functions for the subsequent covalent cross-linking click reaction. Then, the organic linker, here $HC(CH_2O(C{=}O)C{\equiv}CH)_3$, binds these remaining azide functions to form a mixed coordination-covalent bridged 2D sheet (called SURMOF-CL). This material can be considered a hybrid between 2D MOF and 2D COF. Then, the zinc-containing units can be washed away using ethylene diaminetetraacetic acid to lead of a 2D COF (SURGEL) that acts as a gel for surface coating and can also provide good cell adhesion.

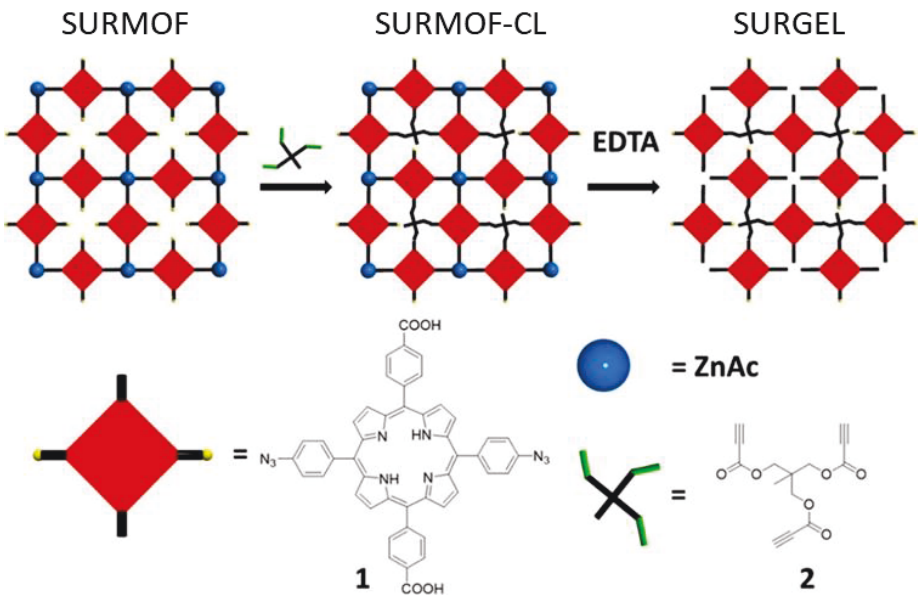

Figure 10. Scheme showing the design of SURMOF and SURGEL. Note that the blue spheres are probably clusters of the type $Zn_4(O)(COO)_6$. Reproduced from ref 78 with permission. Copyright 2018 American Chemical Society.

The endeavour of eradicating bacteria is not without challenges. There is a wide range of *bacterium* on earth and many develop antibacterial resistance with time and sometimes poor management. Among the current potential challenges of antibiotics, there are the arrangement of the bacteria cell walls, severe allergic reactions to the drug, and drug rejection. Alternatively, antibacterial photodynamic therapy, aPDT (*i.e.* generation of $O_2(^1\Delta_g)$ in a biological environment), operates by disrupting the bacteria cell membranes, and appears rather promising. However, the efficiency of the porphyrin-based photocatalyst employed depends on their structure. The structure-property relationship is well documented for molecular porphyrin and metalloporphyrin photosensitizers as such, mainly targeting the Gram-positive and Gram-negative bacteria,[79] but not for porphyrin-based MOFs and COFs. Thus, the search for the discovery of the most effective porphyrin-based MOF and COF photosensitisers is currently undergoing intense research. In the context of this review, the term drug implies the photosensitizer with its various components including composites (MOF or COF physiosorbed to a non-innocent inorganic or organic nanomaterial). The use of porphyrin-based 2D- and 3D-MOFs and COFs as photosensitizers, catalysts or simply platform containing other residues for the eradication of bacteria has indeed experienced an impressive boom in the past few years.[78,80–94] Applications in plant management

have also been reported, which represents a new topic of research for MOFs.[83] Additionally, some MOFs were also used as sensors of drug resistant bacteria using PCN-224 (the structure is shown in **Figure 9**).[93]

The MOF-composites built with conducting or semi-conducting materials exhibit heterojunction features, which opens the door to supplementary redox processes leading to the generation of parallel reactive oxygen species (Type I ROS; $HO^{\bullet}$ and $O_2^{\bullet -}$). These processes are illustrated in **Figure 11**. Depending on the size and geometry of the components or the synthesis procedures, the nanocomposites can be of various designs as shown in **Figure 11** for example. The nanosized MOFs can be smaller than the substrate and can be located on a larger particle or on a surface,[95–99] or small nanoparticles can be located inside the pores [100,101] or simply lying on a larger MOF particle (see below [81]). It is noteworthy that **Figure 11** shows the case where the NPs are electron donors. The situation where porphyrin unit acts as the electron donor also exists.[61,102]

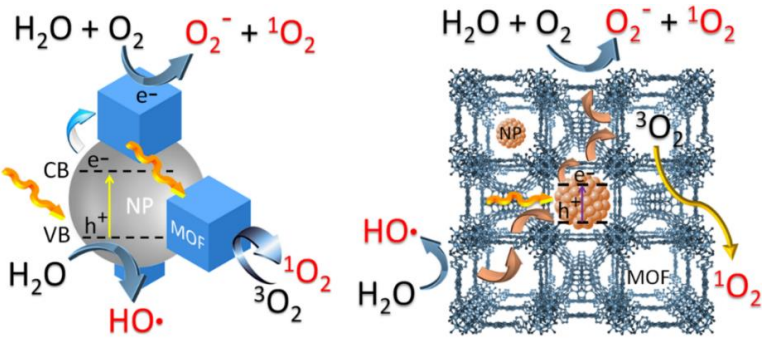

Figure 11. Scheme showing nanocomposites consisting of a semiconducting nanoparticle (NP) that can transfer an electron to the porphyrin-based MOFs, whether is placed outside (due to its size; left) or inside the MOF (right). CB = conduction band; VB = valence band. The ROS are in red.

The incorporation of a nanoparticle inside the pores of a MOF is a common design in composites fabrication. One example consists of preparing Ag nanoparticles using $AgNO_3$ as precursor first and adding them to the solvolysis mixture of the MOF Cu-TCPP.[83] The ligand Cu-TCPP was also prepared separately for comparison purposes. The resulting materials appeared as granular based on SEM and TEM (Scanning and Transmission Electron Microscopy) images with dimensions ranging from 500 to 800 nm (TEM) for both Cu-TCPP and 550 to 600 nm for Cu-TCPP@Ag NPs (SEM). No Ag NPs were observed on the outside faces of the nano-MOF. Elemental composition attested the presence of Ag in Cu-TCPP@Ag and the powder XRD patterns were identical in both

cases indicating that the Ag NPs are encapsulated inside the MOFs, and that the silver ions could not serve as nodes. The comparison of the UV-vis spectra of Cu-TCPP and Cu-TCPP@Ag NPs also confirm encapsulation (slight shift of the Soret and Q-bands). *In vitro* antibacterial properties were assessed against cultures of *S. aureus, E. coli,* and *Bacillus subtilis* with colony-forming unit (CFU) assay measurements, compared to Ag NPs alone, silver ions and penicillin, without irradiation. The antibacterial effect was noticed for Ag NPs, Ag(I) ions, penicillin and Cu-TCPP@Ag NPs) with similar and modest inhibition rates (~55-75 %) after an incubation of 24 h, indicating that silver atoms must leach out of the MOF frame. The main conclusion is that in addition to the synergic effect that NPs can provide when using irradiation (as shown in **Figure 11**, right), the cytotoxicity of Ag can also contribute to the antibacterial property of the MOF@Ag's. This strategy is also viable for MOFs loaded with organics. For instance, naringin-loaded MOFs (MOFs prepared from H_2TCPP, $ZrCl_4$, acetic acid and DMF) and were tested against *S. aureus* with some success.[83] The important information is that the leaching process takes place over multiple hours and days, which contrasts with the approach of using the porphyrin-based MOF, not only as a carrier but mainly as a sensitizer for generation of ROS.

The antibacterial properties are generally addressed by cultivating bacteria in a culture medium, such as agar plates, and the number of produced colonies are counted. The antibacterial efficiency is given by equation 5 (note that treatment could also mean irradiation:

$$\text{Efficiency} = \frac{\text{(number of bacterial colonies in each group under treatment)}}{\text{(number of bacterial colonies in control group kept in the dark)}} \times 100\% \qquad (5)$$

5. Photoinduced antibacterial properties of porphyrin-based MOFs

The most common bacterial species in wound infections are *Staphylococcus aureus* (*S. aureus*) a common food-borne pathogen that is a parasite on the skin, and *Escherichia coli* (*E. coli*) generally found in the lower intestine of warm-blooded organisms. The former is often responsible for severe sepsis, while the latter is known for being able to damage blood vessels as well as the heart. However, poor use of antibiotics helps render these species drug resistant, in addition to their undesired toxicity as a side effect. Consequently, antibacterial photodynamic therapy, aPDT, is an attractive alternative to antibiotics in many circumstances, such as the healing process of wounds. **Table 1** summarizes the list of investigations concerned with aPDT using porphyrin-based MOFs and COFs.

Table 1. Various studies on antibacterial properties of various MOFs and COFs.

pathogens	MOFs	specific topics (key words)	Ref.
E. coli, A. baumannii, multi-drug resistant *E. coli* and *A. baumannii,* methicillin-resistant *Staphylococcus epidermidis*	PCN-224(Zr/Ti)	nanosized, electrospinning with lactic-co-glycolic acid, dressing, *in vivo* study, wound healing evaluation	92
S. aureus, planktonic bacteria	PCN-224@CeO_2	PCN-224@CeO_2/ATP, nanosized composites, bacterial biofilm,	87
E. coli, S. aureus	Hf^{4+} + TCPP→MOF and MOF@MnO_2	bacterial biofilms, *in vivo* study, function-adaptive nanoplatform	80
Staphylococcus aureus	PCN-224@Ag	nanosized, neutrophil membrane coating	94
S. aureus, E. coli	PCN-224(Cu_x) x=5-25	nanosized	91
S. aureus, E. coli	ZPM@Ag	nanosized ZPM (= PCN-224),	81
S. sclerotiorum, P. syringae pv. *Lachrymans*, *C. michiganense* subsp. *Michiganense*, *A. cepa*	Zn-TMPyP@HKUST-1[a]	nanosized antifungal and antibacterial activities	83
S. aureus, E. coli	Ti_3C_2@PCN-224	Ti_3C_2 MXene, nanosheets	82
E. coli, drug resistant *E. coli*	PCN-224(Zr)@chitosan	surface modification	93
E. coli, S. aureus, Pseudomonas aeruginosa, Bacillus subtilis	PCN-224	*in situ* endow woven cotton fabrics	84
S. aureus, E. coli	PB@(UIO-66)@TCPP	Prussian blue (PB), nanosized composite	90
X. Campestris, P. Syringae, A. Alternate [a]	PCN-224, Tebuc@PCN@P@C	Antifungal and antibacterial activity	103

pathogens	COF	specific topics (key words)	
Escherichia coli	2D-TPP	gel, surface coating	78
Pseudomonas aeruginosa *Enterococcus faecalis*	2D-TPP (~COF-366) 3D-TPP, 3D-PdTPP	polystyrene film, antibacterial coating, bacterial biofilm	85
Escherichia coli	2D-TPP	electro-polymerization carbazole, C_{60}	104
S. aureus, E. coli	2D-TAPP+Dha [b]	adsorbed on a membrane, + ibuprofen	86

(a) *S. sclerotiorum,* and *A. Alternate* are fungi.
(b) TMPyP = 5,10,15,20-tetrakis(1-methyl-4-pyridinio)porphyrin place inside HKUST-1.
(c) TAPP = 5,10,15,20-tetrakis(4-aminophenyl)porphyrin, Dha = dihydroxyterephthaldeyde

5.1. Porphyrin photosensitizers as guest molecules inside MOFs

The simplest way to functionalize a MOF is by doping it with a sensitizer. This is performed during solvolysis of the MOF. A recent example involves the sensitizer 5,10,15, 20-tetrakis(1-methyl-4-pyridinio)porphyrintetra(p-toluenesulfonate), TMPyP, and zinc(II)benzene -1,3,5-tricarboxylate, HKUST-1 forming a nano-MOF HKUST-1@Zn-TMPyP.[83] The resulting green colored materials consist of globular nanoparticles of 50-120 nm dimensions (averaging ~79 nm) based on SEM and TEM images. The powder XRD results confirmed the lattice parameters associated with the HKUST-1 lattice. In this case, TMPyP served as template during crystallization but zinc(II) coordinated to the TMPyP ligand in the process as revealed but the position of the Soret band at 438 nm. Colorimetric measurements of DPBF provided evidence for

the formation of $O_2(^1\Delta_g)$ during irradiation (λ_{exc} = 418 nm) of a suspension of HKUST-1@Zn-TMPyP where over 80% of the indicator was consumed in only 4 min (irradiance 6.0 Wcm^{-2}, energy 2.88 J cm^{-2}), and only 90 sec when using a 660 nm laser at a power of 100 mW cm^{-2}. Cultures of plant pathogens *S. sclerotiorum, P. syringae* pv. *Lachrymans*, and *C. michiganense* subsp. *Michiganense* were examined *in vitro* against HKUST-1@Zn-TMPyP for aPDT activities. The HKUST-1@Zn-TMPyP with a loading of 12% (w/w) showed an excellent antibacterial activity. A control efficacity in a pot experiment using *S. sclerotiorum* as a representative example was performed. The cucumber leaves treated with HKUST-1@Zn-TMPyP exhibited a significant inhibition of bacteria, an inhibition that compared favorably with the commercial dimethachlon fungicide under high dosage (**Figure 12**).

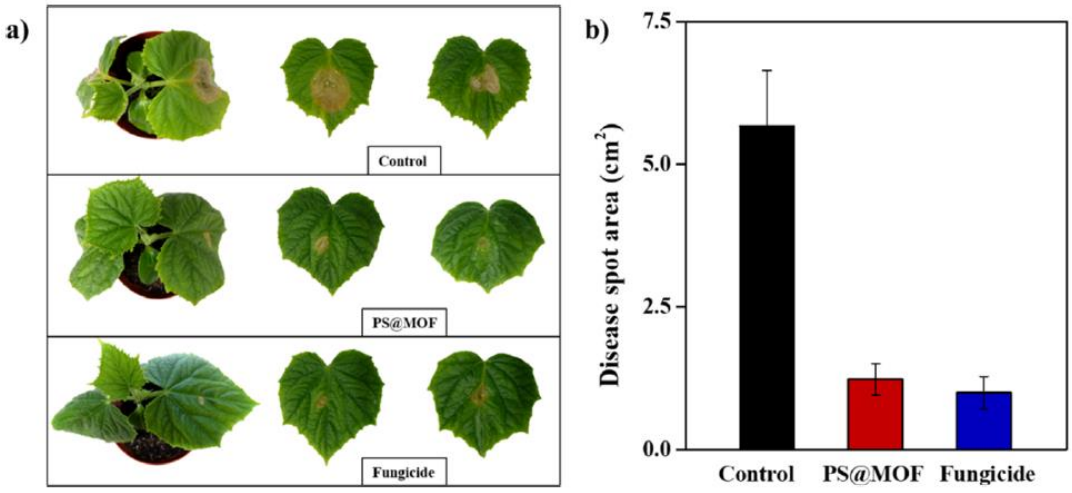

Figure 12. (a) Photos of disease spots on cucumber leaves treated with water (control), PS@MOF, and dimethachlon as commercial fungicide. (b) Comparison of the disease spot area of cucumber leaf infected by *S. sclerotiorum* between water (control), PS@MOF and dimethachlon. The bars are the standard deviation (±SD). Reproduced from ref 81 with permission. Copyright 2021 American Chemical Society.

Stimuli-responsive microcapsules (Tebuc@PCN@P@C: Tebuc = tebuconazole as guest fungicide; PCN = PCN-224 as host; P = pectin; C = chitosan) were used against *Xanthomonas campestris pv. campestris, Pseudomonas syringae pv. Tomato and Alternaria alternate*.[103] In this case, at pH ≤ 5, the MOF releases the fungicide, and under visible light irradiation, the MOF produces $^1O_2(^1\Delta_g)$.

Another interesting three-component nanohybrid was recently designed.[90] This triad consists of nanocrystal of Prussian blue coated by IUO-66 ($Zr_6(OH)_4(O)_4(O_2C\text{-}C_6H_4\text{-}CO_2)_6$) serving as a co-redox surface, which is also doped with H_2TCPP used as sensitizer (**Figure 13**).

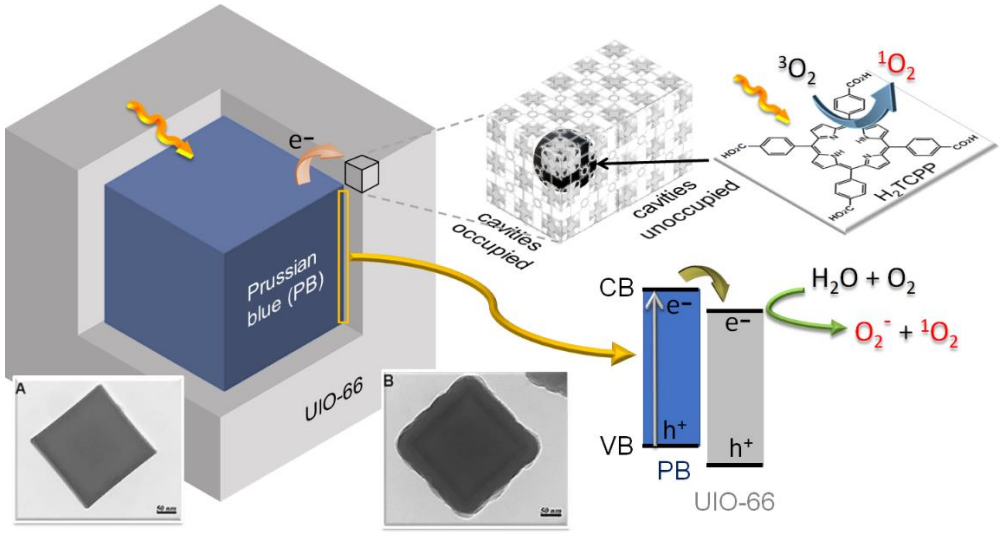

Figure 13. Scheme showing the design of the tri-composite PB@(UIO-66)@TCPP and the electron transfer process PB* → UIO-66. Insets: TEM images of PB (A) and PB@(UIO-66). Reproduced from ref 90 with permission. Copyright 2019 American Chemical Society.

This nano-construction benefits from a dual action of Type I ROSI generation, and perhaps type I as well. SEM images indicates that the nanocubes are of ~260 nm dimensions. IR and powder XRD confirmed the presence of the different phases, including the presence of doped UIO-66. The presence of doping (H_2TCPP) was demonstrated by NMR and the ratio between terephthalic acid and H_2TCPP is 32:1 meaning that only a partial filling of the cavities occurred. The surface area was 362.3 m^2g^{-1}, and the pore size distribution centered at 2.64 nm for the nanocomposite (BET). Prussian blue absorbs in the near-IR region, and H_2TCPP exhibits a strong absorption at 420 nm (Soret band). In this case, the photoluminescence results from a recombination of the free charge carriers and transient photocurrent was indeed detected. Evidence for the production of $O_2(^1\Delta_g)$ was obtained from colorimetric experiments with PDBF while exciting at 660 nm (*i.e.* in the Q-bands of the porphyrin chromophore). Indeed, the yield of $O_2(^1\Delta_g)$ formation increases with the doping concentration. Concurrently, excitation at 808 nm (in the Prussian blue absorption band) does not produce very much, but induces a large temperature increase, which promotes

thermotherapy. Both separate irradiations (λ_{exc} = 660 nm *vs.* 808 nm) give similar antibacterial efficiencies against *E. coli* and *E. aureus*, but combined, the efficiency can reach ~99%.

5.2. Metalation of porphyrins

The metalation of the free base porphyrin-based MOF, such as PCN-224, can serve multiple functions. For instance, in addition to the sensitizer properties of the porphyrin ring, the coordination of Cu(II) ion can trap electrons while under irradiation, which can then supresses electron-hole recombination. Moreover, the doping of Cu(II) ions ($3d^9$) can also promote photothermal properties due to the presence of a low-lying d-d states. In a recent study, such Cu-PCN-224 were prepared by introducing variable amounts of $CuCl_2$ in solutions containing the MOF (130◦C, 10 hr, in DMF).[91] The resulting dark red crystals were characterized by SEM, TEM, elemental mapping, dynamic light scattering, powder XRD, IR, X-ray photoelectron spectroscopy. Evidence for $O_2(^1\Delta_g)$ generation was obtained using DPBF as indicator and by spin trapping with TEMP and EPR spectroscopy. Photothermal properties were highlighted with a thermal camera. The metal coordination did not change the lattice phase and the BET traces were found to be nearly identical regardless of the doping level, while the elemental mapping images (TEM) revealed the correct expected doping level ranging from 4 to 18.6 % (Cu *vs.* Zr) according to ICP-MS. The dimension and the morphology of the nanocubes remain intact as well. X-ray photoelectron spectroscopy showed that the oxidation state of Cu is +2. Copper(II) porphyrins are not emissive so that the overall fluorescence of the free bases within the MOF appears weaker. The system is more complex as the zirconium cluster ($Zr_6(\mu_3\text{-})_4(\mu_3\text{-OH})_4(OH)_4(H_2O)_4(COO)_8$; for instance in PCN-222) may also act as an electron acceptor and H_2TCPP as the electron donor.[60] Nonetheless, holes and electrons are created as well demonstrated by the presence of photocurrent. Upon irradiation, the temperature of the Cu-MOFs raised to 48◦C in 5 min. Cultures of *S. aureus* and *E. coli* were tested against PCN-224, and the various Cu-PCN-224's and clear growth inhibition was observed when the cultures were irradiated. The best results were obtained for the MOF that exhibited a Cu/Zr ratio of 9.2:100 with an efficiency reaching 99.7%. SEM images showed clear evidence for cell membrane collapses for both bacteria upon treatment with MOFs under irradiation (λ_{exc} = 660 nm, 0.4 Wcm^{-2}). The combination of photothermal therapy and aDPT turned out a very good synergy (**Figure 14**).

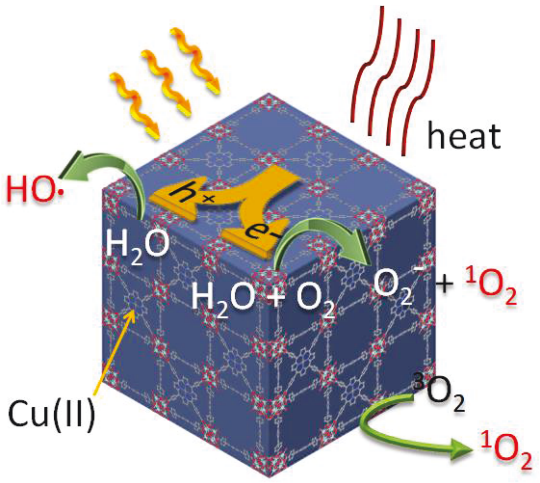

Figure 14. Synergic mechanism for the antibacterial properties of such Cu-PCN-224.

5.3. Post-functionalization of MOFs

5.3.1. Decorated MOFs with nanoparticles

A similar approach was recently used to inhibit biofilms, which is known to be one of the causes of antibiotic resistance and medical complications. This biofilm formation occurs through stimulating cell lysis and extracellular DNA release, and adenosine triphosphate (ATP), which is used a signal transmission in monocellular organisms, plays an important role in the biofilm formation. A dual action can easily be activated by decorating nano-MOFs with CeO_2.[87] CeO_2 NPs (and lanthanide in general) are also known to inhibit biofilm formation through the coordination of ATP molecules with Ce^{4+}. Combined with a porphyrin-based MOF, such as PCN-224, both the photo-induced generation of ROS (causing eradication of bacteria) and ATP deprivation, occur. In this study, PCN-222 nanomaterials were prepared, and the resulting morphology consisted of spheres of 170 nm diameter (TEM). Upon hydrolysis of Ce^{3+} ions, CeO_2 NPs deposited onto the nano-MOF. The resulting PCN-224@CeO_2 nanospheres exhibited an average diameter of 190 nm (TEM). TEM elemental mapping and energy dispersive spectroscopy (EDS) corroborated the presence of Ce atom onto the MOF. Powder XRD patterns confirmed the presence of both the PCN-224 lattice and CeO_2 in its fluorite phase. The oxidation state Ce^{4+} was demonstrated by X-ray photon electron spectroscopy. ICP-MS indicated that the Ce loading was 30% (w/w). DCFH (2,7-dichlorofluorescein) was used as a fluorescing probe to verify that ROS was formed upon light irradiation at 638 nm (0.65 W cm^{-2}) and the quantity of generated ROS was similar for PCN-224 and PCN-224@CeO_2. The key feature is that dead cells do not release ATP. Indeed, the

monitoring of the biofilm biomass upon crystal staining (monitored at 595 nm) indicated that the biomass varies: PCN-224 in the dark > PCN-224@CeO_2 in the dark > PCN-224 with light > PCN-224@CeO_2 with light, thus demonstrating a clear synergy between the two actions. Concurrently, colonies of bacteria (*S. aureus*) harvested from infected tissues on Kunming mice under different treatments were also examined (**Figure 15**). The death cells were maximum with PCN-224@CeO_2 under exposition to light (last frame), thus contrasting to the petri dish kept in the dark.

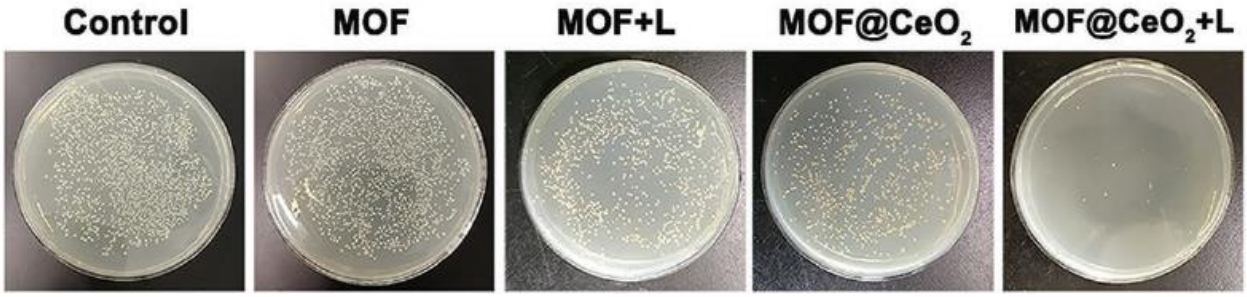

Figure 15. Images of colonies of S. aureus exposed to different antibacterial conditions (L = light). Reproduced from ref 87 with permission. Copyright 2019 Wiley-VCH.

A nanohybrid ZPM@Ag (ZMP = PCN-224; Ag = Ag NPs immobilized at the surface of the MOF), were prepared according to **Figure 16**.[81] Transmission electron microscope (TEM) and scanning electron microscope (SEM) images reveal that the size of the microporous MOF particles (pore diameter = 2 nm; BET 1440 m^2 g^{-1}) is ~1 mm x 400 nm. The use of metallic silver amplifies the antibacterial properties of these nonhybrids. Further analyses were performed (elemental mapping by SEM, FT-IR, powder XRD, X-ray photoelectron spectroscopy (XPS), UV–vis diffuse reflectance and fluorescence spectroscopy). The Ag NPs were of the 1 nm size and XPS revealed the presence of both Ag(I) and Ag(0). The presence of a charge separation upon irradiation was deduced by the weak fluorescence intensity, where the Ag NPs acted electron sinks. Both DMPO and TEMP were used to identify the Type I ROS and II, and indeed EPR spectra revealed evidence for trapped DMPO-O_2^- and TEMP-$^1O_2$. The antimicrobial activity of pristine ZPM, ZPM + Ag and ZPM@Ag nanohybrids was examined and compared using confocal fluorescent images of cultured *E. coli* and *E. aureus* colonies at 37◦C. Upon a 30 min irradiation with visible light, the fluorescence of the stained bacteria turned off entirely for *E. coli* and almost entirely for *E. aureus* witnessing cell death. The cell death was confirmed by SEM images where the cell structure collapsed upon death (**Figure 17**, left). The ZPM@Ag nanohybrids showed the best results

demonstrating the synergic action between the porphyrin-based MOF/Ag NP composite. Together, they form a heterojunction composite (**Figure 11**) where an electron from the valence band (VB) of ZPM is promoted to the conduction band (CB) of the MOF (**Figure 16**). Then, an electron transfer MOF → Ag NP occurs, thus separating the hole (h^+) from the charge (e^-). These species generate the type I ROS, while direct excitation of ZPM forms the type II ROS ($O_2(^1\Delta_g)$, aPDT). The combined action leads to better performances.

Figure 16. Scheme showing the conceptual design of the nanohybrid ZPM@Ag. The MOFs were prepared from H_2TCPP and $ZrCl_4$ with benzoic acid in DMF under solvothermal conditions. Then, the Ag NPs were added to the MOFs upon mixing them with $AgNO_3$ in water at 80°C.[81]

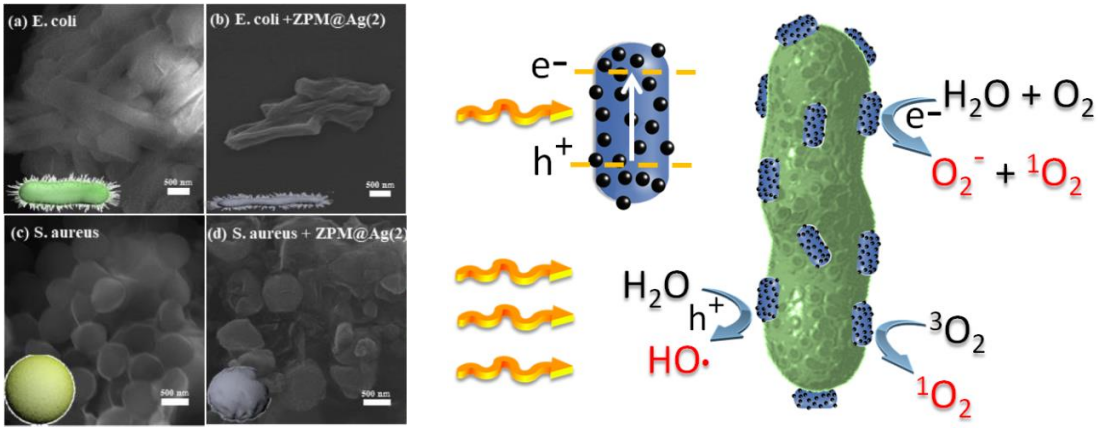

Figure 17. Left: SEM images of untreated E. coli (a) and S. aureus(c), the bacteria E. coli (b), S. aureus (d) treated with ZPM@Ag under visible light illumination for 30 min. Reproduced from ref 81 with permission. Copyright 2021 Elsevier. Right: scheme showing the antibacterial processes.

The photogeneration of ROS is desired as it plays a major role in the collapse of the cell wall of the bacteria and therefore sterilization of a desired surface. The oxidizing ability of $O_2(^1\Delta_g)$ can also be exploited by oxidizing Ag metals into cytotoxic Ag^+ ions, which can leach out faster. In an elaborated study, a porphyrin-based nano-MOF was prepared through solvothermal method using

$ZrOCl_2 \cdot 8H_2O$ and H_2TCPP and benzoic acid via ultrasound, and then kept at 90◦C for 6 hr.[94] The size of these nano-MOF was ~140 nm (TEM images) and powder XRD patterns confirmed the presence of PCN-224. These nano-PCNs were then decorated with Ag NPs upon reducing $AgNO_3$ in a solution containing as-synthesized nano-MOFs in DMF. TEM images revealed the presence of small islands of Ag NPs onto the MOFs (total dimension ~200nm) and powder XRD patterns showed the same signature as that of PCN, plus peaks associated with Ag NPs, which was also confirmed by elemental mapping. Then, the nano-PCNs were coated with mature neutrophils (N), a form of granulocytes of the immune system, to form N@PCN@Ag (**Figure 18**). SEM images confirmed the successful coating (dimension ~220 nm). The presence of photogenerated of $O_2(^1\Delta_g)$ was demonstrated by the change in fluorescence of dichlorofluorescin and SOSG (see structure in **Figure 5**) upon exposing the dyes to the various materials and control with irradiation (λ_{exc} = 660 nm). This property was accompanied by a release of Ag^+ ions upon reaction between Ag and $O_2(^1\Delta_g)$. The side product is not mentioned but $O_2^{\bullet -}$ is reasonably suspected [81] and would enhance the nanocomposite's toxicity. The best performance was obtained for N@PCN@Ag by comparison with N@PCN (PCN coated with neutrophil with no Ag NP) for both $O_2(^1\Delta_g)$ generation and Ag^+ release. *S. aureus* was used to test these materials, and again, this stimuli-responsive N@PCN@Ag composite under irradiation showed the best results, even over N@PCN, well demonstrating the synergic effect.

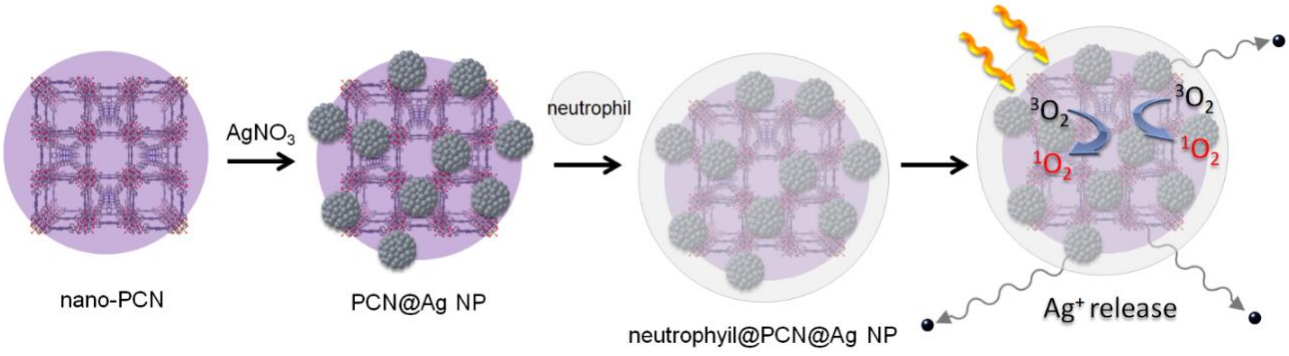

Figure 18. Scheme showing the preparation of nanocomposite N@PCN@Ag (N = neutrophil).

A recent study exploting a double post-functionalisation of PCN-224 involves the formation of heterojunctions with MnO_2 clusters coated with a biocompatible membrane human serum albumin (HAS).[80] The porphyrin-based MOF built with Hf^{4+} ions, PCN-224(Hf), was previously reported and is found isomorph to the commonly used PCN-224 built with Zr^{4+} ion (upon comparing the

powder XRD patterns) [105] and was resused in this study. Hf^{4+} ions exhibit strong X-ray attenuation and often serve as a radio-sensitizer to enhance radiotherapy in cancer treatment.[105,106] The key role of HAS is to permit the nanocomposites to penetrate through the biofilm formed by the bacteria more easily. To ease this penetration further, the size of the NPs of PCN-224(Hf) were sonicated to form dots of ~5 nm (TEM images). This small dimension permits convenient rapid escape from the MOF when considering that the $O_2(^1\Delta_g)$ lifetime is in the μs time scale. The identity of the MOF lattice was confirmed from the powder XRD patterns and AFM images indicated that the topographic average diameter was 4.7 nm. Upon exposing these dots to HAS-coated MnO_2 clusters, the resulting particles anchored the MnO_2 clusters at its surfaces under alkaline conditions and were characterized as multicomponent nanoplatforms (MMNPs) in this study exhibiting a hydrodynamic size of 105 nm and are positively charge rendering them more prone to attach to the acidic cell wall of the bacteria. The presence of both Mn and Hf elements was confirmed by TEM elemental mappings of the MMNPs. These MnO_2 clusters are pH-responsive. Under acidic environment such as inside the biofilms formed by the bacteria (pH ~ 5.5), the presence of H^+ ions trigger the decomposition of MnO_2 and release O_2, thus securing a continuous supply of O_2. It is noteworthy that when $O_2(^1\Delta_g)$ reacts with cell membrane, the resulting oxidized products contain oxygen atoms, thus rapidly and irreversibly consuming O_2 inside the biofilm, so photosensitisation stops. The concept is summarized in **Figure 19**.

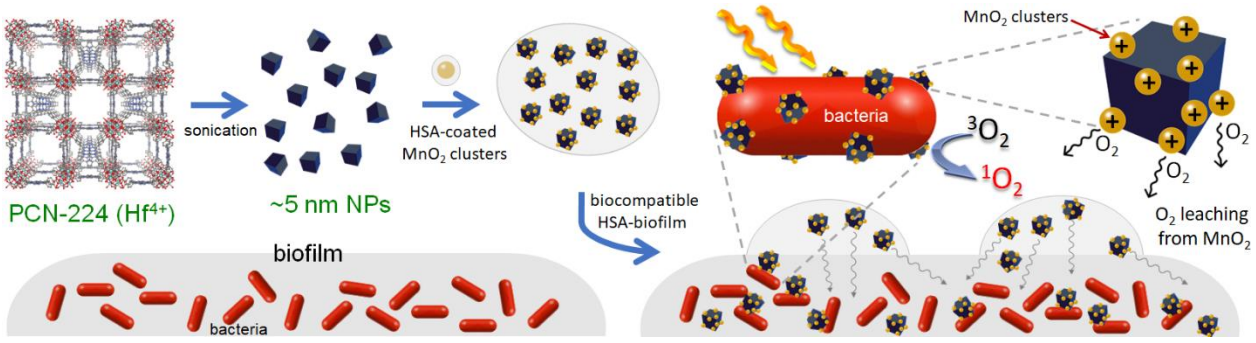

Figure 19. Scheme showing the preparation of the MMNPs and their penetration processes in biofilms according to reference 80.

Their antibacterial efficiencies against *E. coli* and *S. aureus* cultures were also evaluated. The percentage survival of these bacteria decreased drastically when the cultures were illuminated. MMNP was also tested *in vivo* for its cytotoxic effect against abscesses with a local infection of *S. aureus*. The nanocomposites were injected subcutaneously into the abscess and irradiated with

visible light. After 5 days of illumination, no obvious inflammation was observed, performing far better than the control group (phosphate buffered saline (PBS), and PBS + light).

5.3.2. Decorated MOFs with biocompatible functions

A pH-responsive MOF was also designed in order to sense drug resistant bacterial infection and to eradicate them at the same time by two possible therapeutic actions.[93] The concept stems from the fact that bacteria generate a microenvironment where pH, toxins and enzymes differ from a healthy one. The change in pH stems from the glycometabolism of most pathogens. Crystal engineering permits the coating of nanoparticles with desired functional groups, in this case a pH-responsive chain: chitosan (**Figure 20**).

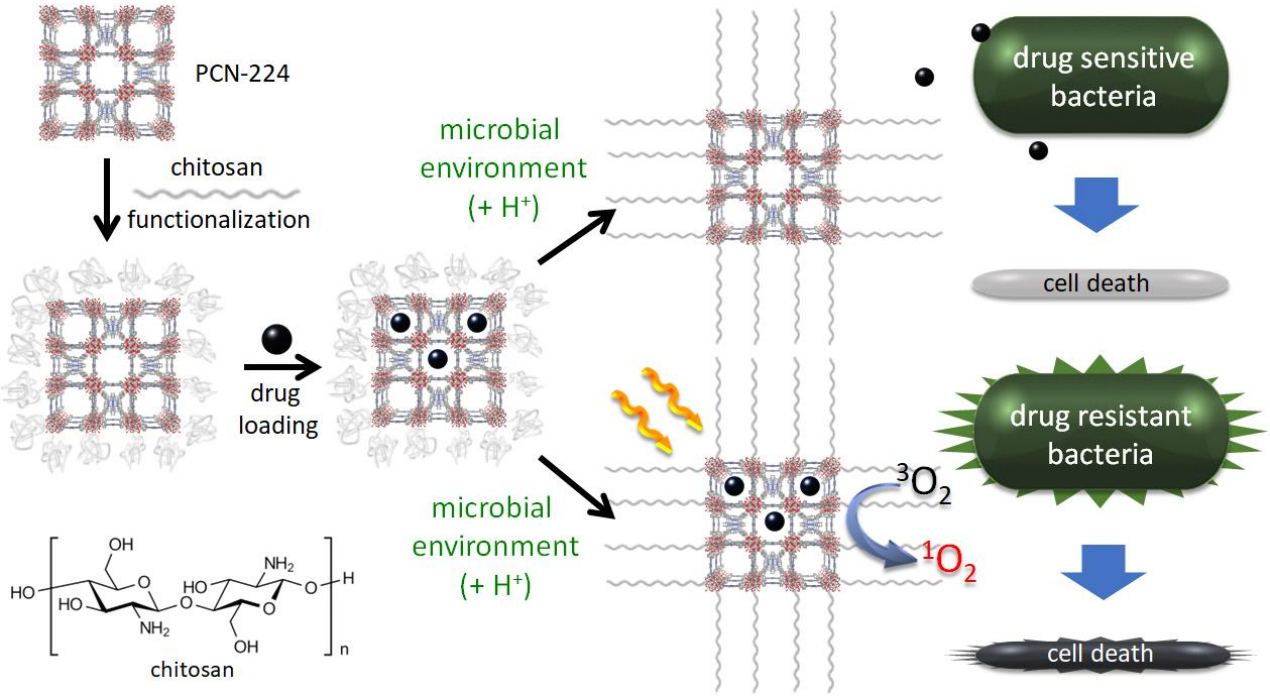

Figure 20. Design of bifunctional antibacterial nano-MOF according to ref 93.

Upon protonation, the positively charged chains repel each other inducing a breakup of the random coil structure to form elongated filaments, thus opening the pores more widely. This process allows for the therapeutic agent to slowly leach out of the MOF where the acid-triggering occurred. The stimuli-controlled release of cargos from a coated MOF is well known in biomedicine.[107,108] In this study, nanosized MOFs of PCN-224 were prepared and from post-synthesis, they were functionalized with chitosan. After loading, the nano-NOF can be then incorporated into a device. In this investigation, the authors anchored the nano-MOFs onto a

surface of paper coated with an indicator to identify whether drug sensitive or drug resistant bacteria were present. Depending on the result, the optional slow release of antibiotics is enough to eradicate the drug sensitive bacteria. However, in the presence of drug resistant bacteria, aPDT is necessary. The latter process is much faster but suffers from limitations due to skin penetration.

5.4. Design of MOF-containing antibacterial fabrics

The design of fabric exhibiting aPDT has also been reported. In this case, a woven cotton fabric (WCF) was used.[84] The fabrication consisted of the preparation of PCN-224 under a standard method (TCPP + $ZrOCl_2$ + benzoic acid in DMF, stirred for 5 hr at 90◦C) in the presence of a piece of WCF (100 x 100 mm; **Figure 21**). The solution was first sonicated for 10 min, then heated for 5 hr at 90◦C. The resulting fabric was washed five times (in DMF and ethanol), and then freeze-dried. The fixation of PCN-224 was verified by SEM images. IR, TEM and powder XRD methods and elemental analysis (EDS) were also employed to confirm the presence of PCN-224 in the fabric. The proportion of weight due to PCN-224 was 9.12%. The stability of the fabric was tested using TGA where a slight weight loss was noted above 100◦C. Cultures of *E. coli, Pseudomonas aeruginosa, S. aureus, and Bacillus subtilis* were bacterial strains used, which were then irradiated for 45 min ($\lambda \geq 420$ nm). The presence of $O_2(^1\Delta_g)$ was confirmed using the colorimetric and fluorescent DPBF indicator. The dark control of the survival rate of the bacteria was compared to those after aPDT. WCF alone shows a very poor inactivation level (<1%). Conversely, an impressive inactivation rate of 99.9999% of inactivation was noted for all four bacteria strains after aPDT. There was no evidence for type I ROS, which is consistent with the absence of redox component.

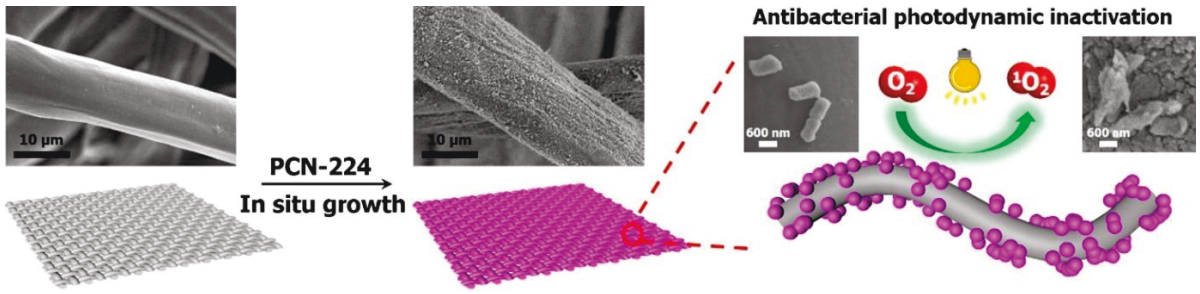

Figure 21. Bottom: cartoon illustrating the fabrication of PCN-224/WCF and aPDT towards *E. coli.*[84] Above are the SEM images of WCF fiber alone (thickness: ~293 μm, 170 gm^{-2}; far left) and PCN-224/WCF (middle), and images showing living E. coli and dead E. coli before and after

aPDT treatment (note the cell wall destruction, far right). Reproduced from ref 84 with permission. Copyright 2020 Elsevier.

Another bifunctional material was designed using PCN-224 and Ti_3C_2 MXene, which respectively exhibit aPDT and photothermal properties.[82] It is noteworthy that 2D-Ti_3C_2 MXene has attracted tremendous attention recently since, among many interesting properties, it is a material that strongly absorbs light all the way in the near-IR region and exhibits efficient light→heat conversion due to localized surface plasmons.[109] Consequently, eradication of bacteria becomes more efficient if heat is combined to ROS attacks. Thus, the combined action of the PCN-224 and Ti_3C_2 MXene composite represents an interesting material for the design of smart fabric knowing that the surface temperature of a photothermal material, then it should increase with elimination time. The only drawback is overheating, which would lead to premature aging of the fabric, and discomfort caused to humans. In this investigation, a cotton fabric was impregnated with a thermochromic dye (45 °C color change, No. TSG-45, Shenzhen Qiansebian New Material Technology Co) acting as an indicator, which turns green when the temperature reaches 45 °C. The procedure for the fabrication of this smart material is shown in **Figure 22** and consists in generating first PCN-224 *in situ* with the fabric inside the reactor. Then, the surface of the fabric was decorated with Ti_3C_2 MXene using electro-spray, and subsequently pasted with a thermochromic dye using the screen-printing technique. Successful synthesis of PCN-224 was confirmed by XRD and generation of $O_2(^1\Delta_g)$ was demonstrated by colorimetry using DPBF. The presence of Ti_3C_2 MXene was verified by XRD, EDS and SEM elemental mapping. The antibacterial inactivation of *E. coli* and *E. aureus* reached an impressive 99.9999% upon irradiation at 780 nm using a near-IR laser and under a visible Xe lamp ($\lambda_{exc} \geq 420$ nm), and the temperature of the fabric also reached nearly 50 °C within 3 min based on an IR camera and the fabric turned green. It is noteworthy that the fabrics loaded with PCN-224 without Ti_3C_2 MXene reached a temperature of 37 °C only.

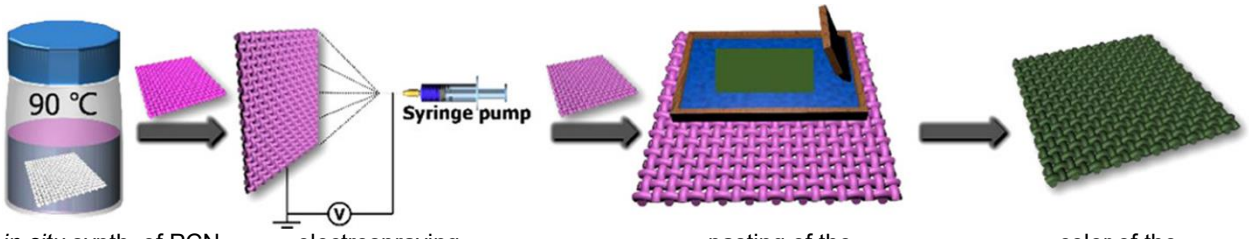

Figure 22. Scheme showing the procedure for the preparation of the fabric containing PCN-225, Ti_3C_2 MXene and the thermochromic dye. Reproduced from ref 82 with permission. Copyright 2021 American Chemical Society.

It is noteworthy that the substitution of the protons inside the porphyrin ring by a copper(II) atom was made to enhance the antibiotic properties of the nano-MOF (PCN-224) discussed above.[91] In this work, one or several zirconium atoms were replaced by titanium(IV) ions.[92] To do so, a certain amount of $TiCp_2Cl_2$ is used as post-synthesis reagent with PCN-224 to form a mixed-metal node MOF: PCN-224(Ti/Zr). The powder XRD patterns remained unchanged compared to that of PCN-224. The XPS spectra and elemental mapping images confirm the presence of both elements inside the nano-MOFs (409.5 ± 10.2 nm). The emission of PCN-224(Ti/Zr) turned out to be weaker than that of the control PCN-224 indicating quenching by photoinduced electron transfer from TCPP to metallic node. The percentage of introduced titanium atoms is 35.87 % based on ICP-OES. The performance for ROS generation was measured using 2'-7'dichlorofluorescin diacetate (DCFH-DA), which emits when in presence of ROS. Under identical experimental conditions, the resulting emission of the DCFH-DA essay with PCN-224(Ti/Zr) was over 3 times more intense than that for PCN-224. *In vitro* testing of the bacterial activity of Gram negative (*E. coli,* drug resistant *E. coli, A. baumannii,* and drug resistant *A. baumannii*) and Gram positive (*E. aureus,* drug resistant *E. aureus, S. epidermidis*) was performed using staining with photoluminescent dyes and SEM to examine the morphology of the non-treated and treated bacteria. After 20 min of irradiation, the plate counting indicated that the elimination efficiency varied between 96 to 98.8%, which is commendable for bacteria such as *A. baumannii* and drug resistant *A. baumannii* are extremely hard-to-treat bacteria. The medical performance of PCN-224(Ti/Zr) for aPDT was evaluated using a dressing applied over a wound. A biodegradable nanofiber (containing poly(lactic-*co*-glucolic acid), PLGA, or not) was fabricated loaded with the MOF (or not) *via* electrospinning (**Figure 23**, left). SEM images confirmed the presence of nano-PCN-224(Ti/Zr) were well encapsulated in the fiber (see white dots in **Figure 23**, middle). Methicillin-resistant *Staphylococcus aureus* (MRSA) and drug resistant *E. coli* were introduced in mice. Wounds were treated with regular gauze, dressings containing only PLGA, and dressings containing nano-PCN-224(Ti/Zr)@PLGA. The dressings and gauzes were irradiated 30 min. Typical photographs of the wound healing progress are shown in **Figure 23**, right. A drastic decrease in size of wounds infected with MRSA and drug resistant *E. coli* is observed with

treatment. The comparison was made against regular gauze, and dressings containing PLGA only (not shown). In conclusion, the titanium incorporation appears to boost the ROS generation and its antibacterial effect, but no biomedical testing was performed using regular PCN-224 as control.

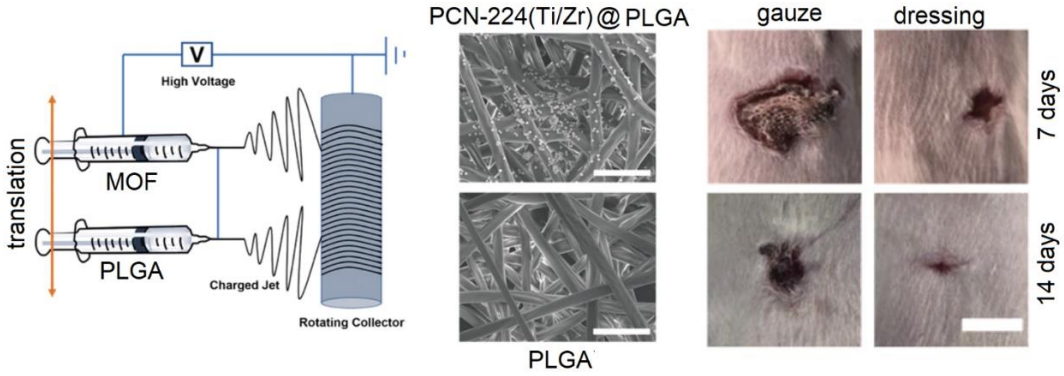

Figure 23. Left: scheme showing the electrospinning device used for the fabrication of PCN-224(Ti/Zr)@PLGA dressing and their control dressings. Middle: SEM images of the dressing network containing PCN-224(Ti/Zr)@PLGA (top) and containing PLGA only (bottom); scar bar = 10 μm. Right: photographs of wounds infected with MRSA for example) for wound healing evaluation for dressings containing PCN-224(Ti/Zr)@PLGA *vs.* gauze only *vs.* dressing containing PCN-224(Ti/Zr)@PLGA after 7 and 14 days; scar bar = 1 cm. Note that the photographs showing wounds treated with the dressing containing PLGA only show similar sizes as the regular gauze. Reprinted in part with permission from ref. 92. Copyright 2010 John Wiley and Sons.

6. Photoinduced antibacterial properties of porphyrin-based COFs

The use of antibacterial COFs targets surfaces (**Figure 24**). There are less characterization methods possible from those used for MOFs due to a generally lower level of crystallinity and absence of metallic nodes. However, in general the nature of the COF materials is well elucidated. IR spectroscopy allows for the monitoring of the functional groups during the fabrication process. UV-vis and fluorescence spectroscopy allows for the confirmation of the presence of porphyrins and assesses as to whether the porphyrin ring has been altered (*i.e.* metalation). COFs are often porous and quartz crystal microbalance may indicate the absorptivity of small molecule vapours and kinetics (QCM sorption experiments). Powder XRD patterns provide a qualitative idea on the level of crystallinity, and SEM images give information on the morphology of the film.

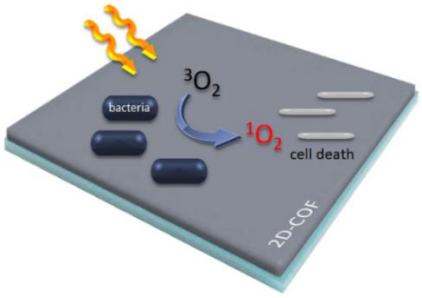

Figure 24. Drawing illustrating the quasi-exclusive of mode of applications of antibacterial COFs.

In the first example, SURGEL (**Figure 10**) was prepared in three steps using a 2D pseudo-MOF called SURMOF.[78] Essentially, SURMOF served as a pre-programmed template providing concurrently a high degree of ordering as demonstrated by XRD. First, epitaxially grown SURMOF is prepared layer-by-layer from subsequent spray coating of the porphyrin precursor with the metal ions and linker (*i.e.* zinc acetate). In the second step, the SURMOF is immersed in a solution containing the organic linker ($HC(CH_2O(C{=}O)C{\equiv}CH)_3$) to induce the click chemistry at 80◦C. Then in the third step, the metal ions are removed using EDTA. The resulting film has a thickness of 400 nm (SEM), which appears to be thicker than necessary considering the sphere of activity of $^1O_2(^1\Delta_g)$ up to 100 nm.[110] The uptake capacity of ethanol vapour for a sample of about 1 μg cm^{-2} was observed (QCM sorption experiments). After characterization, the photoinduced $^1O_2(^1\Delta_g)$ generation by SURGEL was verified by colorimetric measurements using anthracene-9,10-dipropionic acid disodium salt as indicator (λ_{exc} = 455 nm). The antibacterial efficiency of SURGEL was evaluated against *E. coli* as model organism. Both fluorescence imaging of stained bacteria and counting colonies in Petri dishes indicated a strong light-induced toxicity. After 1.5 hr of irradiation using visible light, the survival percentage of the bacteria was 2.29% compared to 79.68 % in the dark in the presence of SURGEL.

There are a limited number of reported 3D-COFs and they are usually prepared using the strategy illustrated in **Figure 8**. Using Schiff-base chemistry, 3D- (**3D-TPP**, **3D-PdTPP**) and 2D-COFs (**2D-TPP**) were synthesized according to **Scheme 4**.[85] It is noteworthy that the presence of terminal -NH_2 groups provides better adhesion to bacterial cell membranes. The ν(C=N) (1260 cm^{-1}) and ν(C=O) (1700 cm^{-1}) IR peaks are good diagnostics of the reaction progression. N_2 sorption measurements (BET) indicate that **3D-TPP**, **3D-PdTPP** and **2D-TPP** are respectively

micro-meso bimodal (pore width D_{max} = 1.2, 9 nm), mesoporous (D_{max} = 7-8 nm) and microporous (D_{max} ~ 2 nm).

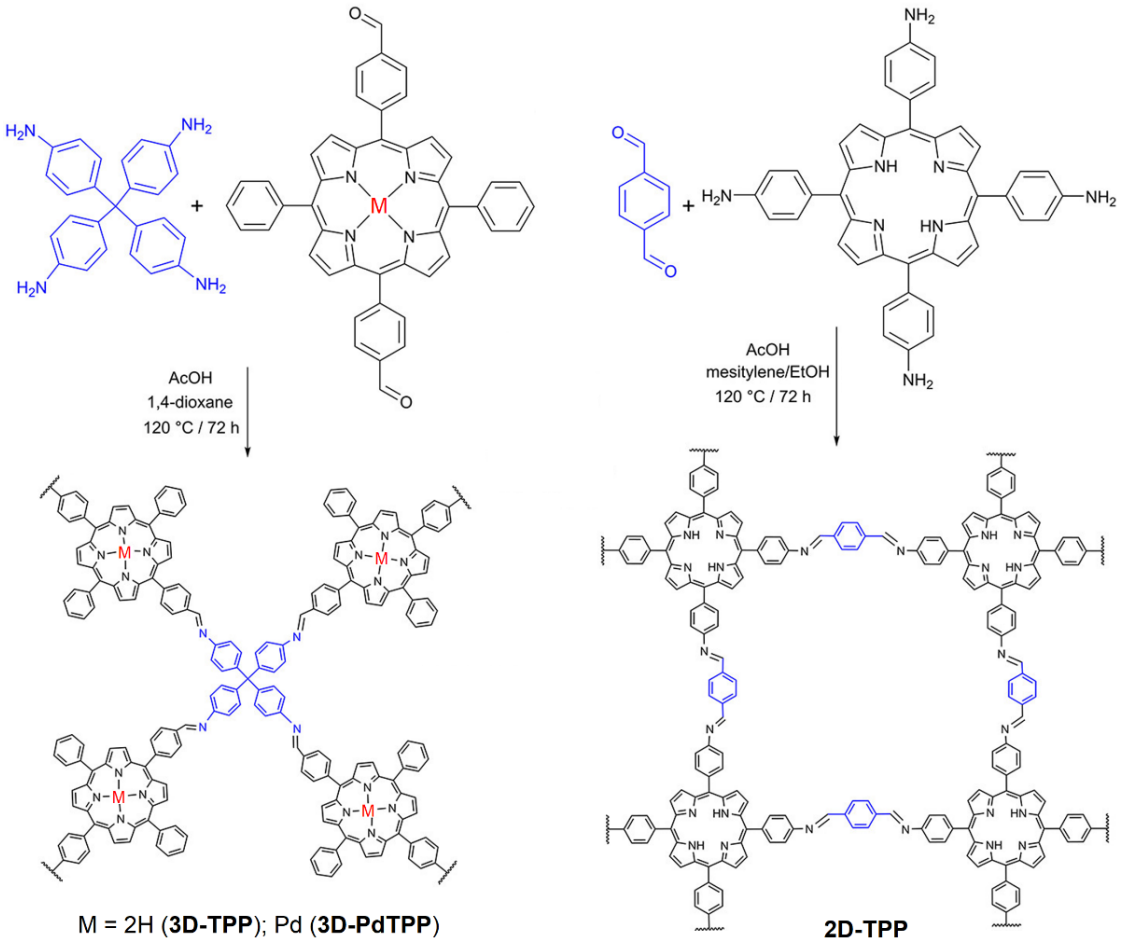

Scheme 4. Synthesis of 3D-TPP, 3D-PdTPP and 2D-TPP. Reproduced from ref 85 with permission. Copyright 2018 American Chemical Society.

2D-COF was used as comparison material which bears resemblance to COF-366.[111] Indeed, the powder XRD pattern of 2D-TPP exhibits diffraction peaks at 2θ = 4.0° and 9.1°, which correspond to an interplanar spacing of 25.2 Å. This value compares favorably with that of COF-366.[111] Conversely, **3D-TPP** and **3D-PdTPP** do not diffract X-ray indicating the absence of crystalline domains. The triplet excited state of the COFs ranges from 200 to 490 μs and the photosensitization of $^1O_2(^1\Delta_g)$ was addressed using 9,10-diphenylanthracene. The order of efficiency is **3D-PdTPP > 3D-TPP > 2D-TPP**, which is consistent with the heavy atom effect populating the triplet state efficiently, and the shorter triplet lifetime of **2D-TPP** (460 μs)

compared to 490 μs for **3D-TPP**. The aPDT properties of these COFs deposited on top of polystyrene were addressed against *pseudomonas aeruginosa* and *enterococcus faecalis*. Both bacterial strains form stable multicell-thick biofilms. The three COFs turned out effective in breaking down the biofilms upon irradiation for 4 hr (λ_{exc} = 460 nm; 1 mW cm^{-2}). The three COFs exhibit high photostability, meaning they are robust even in the presence of ROS, especially **3D-PDTPP**.

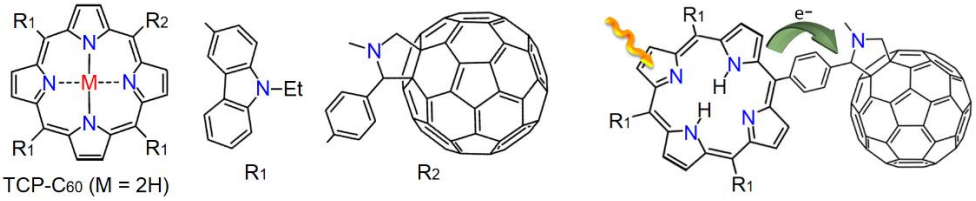

Figure 25. Left: structure of **TCP-C$_{60}$**. Right: illustration of the photo-induced electron transfer generating the charge separated state responsible for forming the superoxide ROS.

Electro-polymerization was used to generate porphyrin-based 2D-COFs using N-ethylcarbazolyl-porphyrin-C_{60} dyad, **TCP-C$_{60}$** (**Figure 25**, left), deposited on a semi-conducting semi-transparent indium tin oxide (ITO) forming a thin electro-active film.[112] Past literature indicates that the oxidation of carbazole occurs at the 3,3'-positions.[113] This dyad is accompanied by **TCP** (M = 2H, R_2 = R_1) and **ZnTCP** (M = Zn, R_2 = R_1) as comparative films. These films exhibit an homogeneous morphology on an ITO electrode. The characteristic absorption peaks of the porphyrin and zincporphyrin attest to the integrity of the dyes in the films and the bathochromic shifting of ~10 nm, in comparison with the solution data, indicates the presence of interporphyrin interactions inside the films. Tetrasodium 2,2-(anthracene-9,10-diyl)bis(methylmalonate) was used as indicator for the photosensitization of $^1O_2(^1\Delta_g)$ through colorimetric experiments and **TCP-C$_{60}$** was found to be the most efficient. The photodegradation of nitro blue tetrazolium into diformazan (λ_{max} = 600 nm) monitored by UV-vis spectroscopy was used to assess the formation of $O_2^{\bullet -}$ in water.[114] Again, the best films were those containing **TCP-C$_{60}$**. Two pathways may explain the production of $O_2^{\bullet -}$. The first one is the creation of a charge separated state (**Figure 25**, right), then $C_{60}^{\bullet -} + O_2(^3\Sigma_g^-) \rightarrow O_2^{\bullet -} + C_{60}$. The second one is $^3C_{60}^* + O_2(^3\Sigma_g^-) \rightarrow O_2^{\bullet -} + C_{60}^{\bullet +}$. Altogether, films containing **TCP-C$_{60}$**. are better at photo-generating ROS. The only potential drawback is that back electron transfer ($C_{60}^{\bullet -}$ to porphyrin$^+$) in the charge separated state in model compounds occurs in the ns time scale.[115–117] This fact means that collision between $O_2(^3\Sigma_g^-)$ and $C_{60}^{\bullet -}$ must

occur within this time window. Considering the amount of O_2 in air at 1 atm (1 mole = 22.4 L) and its velocity (461 m s^{-1} at STP), this should not be a major issue at the surface of the film. However, inside the bulk of a thick electro-generated film (many hundreds of nm), it could be. *In vitro* inactivation of *S. aureus* and *E. coli* by films containing **TCP**, **ZnTCP** and **TCP-C_{60}**, was tested. The best films were those containing **TCP-C_{60}** (up to 99.97% of inactivation for 30 min of irradiation of visible light). This outcome is consistent with the findings on the ROS production experiments. The films containing **TCP** and **ZnTCP** were less active.

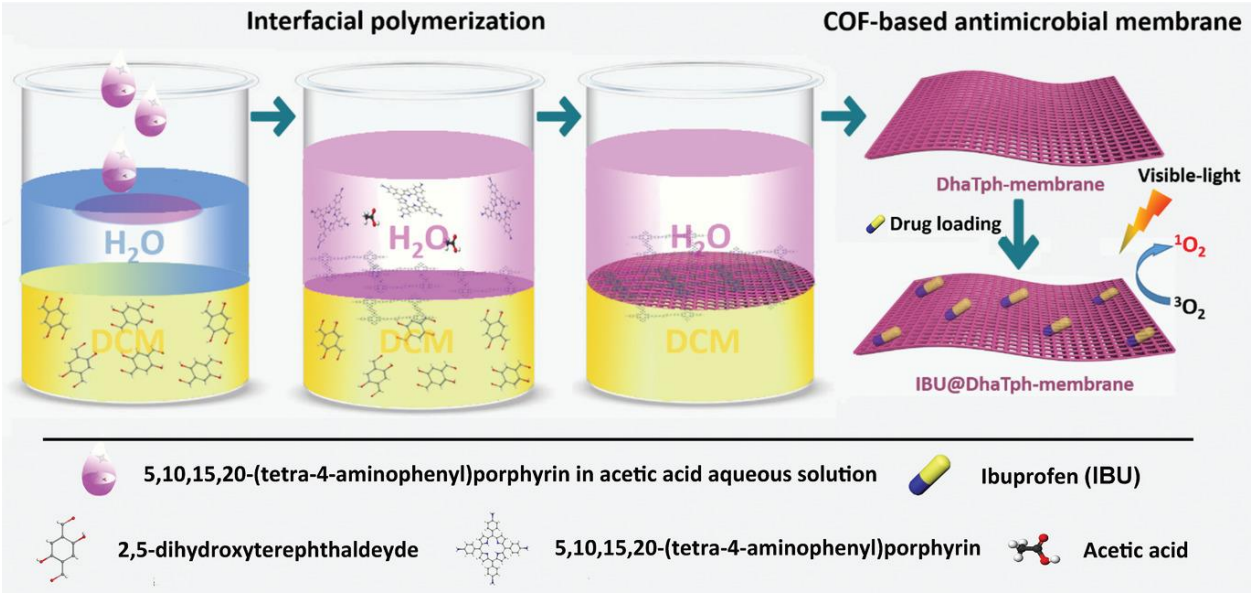

Figure 26. Scheme showing the preparation of the multifunctional membrane containing the porphyrin-based COF and ibuprofen. Reproduced from ref 86 with permission. Copyright 2021 Wiley-VCH.

The impregnation of a photo-sensitizer porphyrin-based COF along with ibuprofen as an anti-inflammatory drug into a membrane, was recently preformed.[86] The preparation of such a membrane is illustrated in **Figure 26**. In this study, 5,10,15,20-tetrakis (4-aminophenyl) porphyrin is subjected to 2,5- dihydroxyterephthaldehyde at a water/CH_2Cl_2 interface to afford a thermally stable (up to 200 °C; TGA), mechanically robust and flexible purple-black material (**DhaTph-membrane**). Characterization was achieved using IR (ν(C=N) = 1612 cm^{-1}) and solid-sate ^{13}C CP-MAS NMR (δ ^{13}C=N = 161 ppm) spectroscopy. High crystallinity materials were obtained as asserted by two diffraction peaks 2θ = 3.4° (Miller indices = 100) and 6.9° (200), which correspond well with those of a parent and well-known COF (**DhaTph**),[118] which is not modified

upon uploading with ibuprofen. N_2 sorption measurements (BET) indicate that the material has a specific area 937.5 m^2 g^{-1}, which decreases (to 499.0 m^2 g^{-1}) upon loading with the drug. This free-standing material can be applied as a band-aid on skin for wound healing applications. The surface topology of the 150 μm thick membrane was examined by ESM and the images showed a homogeneous texture (height variation = ± 6 nm). This membrane exhibits the expected spectral signature in the UV-vis spectra of porphyrin chromophore, which efficiently photosensitize $^1O_2(^1\Delta_g)$ ($\lambda_{exc} \geq 400$ nm, ~52 mW cm^{-2}) as monitored by the photooxidation of DPBF. The spin-trapping of $^1O_2(^1\Delta_g)$ was also performed using TEMP and EPR spectroscopy to corroborate the photobleaching experiments. The antibacterial properties of **DhaTph-membrane** were verified against *S. aureus* and *E. coli* under both visible light and sun light, which gave similar results. The bacterial survival rate decreased to 4.1% and 5.8% for *S. aureus* and *E. coli*, respectively, for an irradiation of 3 h. Wound healing tests on mice infected with *S. aureus* were performed. Almost complete healing of ~8 mm wound was observed for mice treated with an ibuprofen-containing **DhaTph-membrane** and sun light (30 min in total) over a period of 14 days. Conversely, the wound in mice treated with **DhaTph-membrane** without ibuprofen showed a 50% reduction in wound size. Experiments conducted in the dark showed no reduction in wound size. All in all, there is a clear synergetic action of the loaded membrane, each (ibuprofen and aPDT) contributing about evenly to the healing.

7. Discussion

The photoinduced eradication of bacteria by molecular porphyrin pigments used as sensitizers is well documented [65,79] and the quest to apply this important sanitisation property to textiles is also not new.[119–122] However, the superiority of the nano-MOFs and nano-COFs versus conventional antibacterial methods has been demonstrated on several occasion. For instance, some nano-MOFs are found environmentally friendly nano-MOFs are found to perform the same task as conventional pesticides with similar efficiencies. Moreover, several nano-MOFs and nano-COFs and composites can eradicate drug resistant bacteria, while conventional drugs fail. It is noteworthy that there is no comparison of efficiencies of MOFs and COFs for their relative antibacterial properties, even though the experimental conditions employed are carefully described, they systematically differ from one another. Comparison with other materials, such as porphyrin-containing polymers,[123,124] while interesting, seems to lay behind significant

experimental hurdles if it is to be done rigorously. This situation contrasts with what is commonly done when evaluating solar cell performances (*i.e.* power conversion efficiency at A.M. 1.5; 1000 W m^{-2}) or when evaluating the quantum yields of sensitized $^1O_2(^1\Delta_g)$ in solution (*i.e.* comparison against a standard with precises experimental conditions). One critical parameter is the size of the nano-MOFs and nano-COFs. Photogenerated $^1O_2(^1\Delta_g)$ at the surface of these nanomaterials or inside, do not have the same antibacterial effect due to the time scale of their lifetimes (μs). This consideration excludes the morphology issues, including degree of porosity for instance. One can also wonder whether optimisation of the photosensitizers, and perhaps the nature of textile, is a worthy investment, particularly when one considers the possibility of using day and room light as the constant source of mild photocatalyst's activation. Standardization of the evaluation of MOFs and COFs antibacterial activities, beyond measurements of quantum yields of generation of $^1O_2(^1\Delta_g)$, appears to be a worthy venture in this field.

Concurrently, this minireview indicates that the use of porphyrin-based MOFs and COFs for this medical purpose is in its infancy and that a significant increasing interest has evolved over the past several years. However, since the solid-state photogeneration of ROS is mainly a surface process (but not exclusively), it appears relevant to compare these 3D- and 2D-scaffoldings with their corresponding 0D-molecular dyes while immobilized on fibers. 3D-MOFs exhibit the clear potential advantage by their much larger specific area in comparison with grafted molecular pigments onto fabrics and reports stated the superiority of MOFs over molecules in terms of $^1O_2(^1\Delta_g)$ generation. Then, one may wonder whether the increased cost of using these nanocarriers (namely the PCNs) is a viable approach. Concurrently, MOFs and COFs have the disadvantage that the generated ROS well inside the MOF and COF nanostructures still must escape the porous particles for efficient action prior to relaxation to the ground state $O_2(^3\Sigma_g^-)$ (*i.e.* by non-radiative means, or by reacting with the pigment itself) if it is to have any beneficial effect.

It is also interesting to note that viricidal properties have also been discovered for porphyrin derivatives using the photosensitizing approach.[125–127] The question is can MOFs and COFs be more efficient at eradicating viruses knowing that the formation of biofilms and cell penetration are not an issue in these cases.

Nanosized composites containing porphyrin-based MOFs for antibacterial applications have been thoroughly explored, and evidence for synergic actions has been unambiguously provided. Concurrently, despite the fact many composites of porphyrin-based COFs have been described

thorough the literature, particularly during the past three years,[95,128–137] composite materials using the photosensitizer porphyrins dedicated for generating ROS has been modestly employed. To the best of our knowledge, only one study reporting a composite material with graphitic carbon nitride (g-C_3N_4@COF) aiming at pollutant destruction in water, appeared.[138] Considering that the efficiencies for photo-induced eradication of bacteria using nanosized composites containing porphyrin-based MOFs are clearly superior (> 99.9%) to those for pristine MOFs and COFs, there seems to be an opportunity for further exploration.

It is well known that arsenic, beryllium, cadmium, hexavalent chromium, lead, and mercury are serious environmental threats and provoke health issues. The described MOFs and COFs herein, along with their composites, are all in the nanometric dimension, and include zinc, zirconium, iron, copper, cerium, manganese, titanium, palladium, silver, and hafnium. For antibacterial textiles for medicinal applications and sanitisation, the disposal of these fabrics after usage may cause a stress on the environment and potentially health issues upon long term exposures. First, nanosized materials are inherently and potentially dangerous due their ability to penetrate living cells. Second, elements or ions, such as silver, copper, titanium carbide, manganese (here as manganese oxide), palladium, and cerium are toxic, especially upon long term exposures. Moreover, iron has a corrosive effect on gastrointestinal mucosa. Conversely, zinc, zirconium, and titanium oxide exhibit very low toxicity. Consequently, PCN-type MOFs seem, at first glance, better suited for daily antibacterial applications and subsequent disposal. The possibility of recycling porphyrin-based MOFs as photocatalysts has also been addressed with some success,[139–141] but for more reactive ROS, namely Fenton-like species (H_2O_2, •OH) degradation may be observed.[142] However, this review indicates that the various investigations on the antibacterial properties did not address this issue, particularly for studies involving the testing of fabrics, surfaces, and membranes. Concurrently, porphyrin-based COFs do not bear a metallic node but may have a coordinated metal inside the porphyrin ring (i.e. zinc [78] or palladium [85]). While the former is harmless, the heavier metal is not. Again, the recycling of COF-photocatalysts is possible.[143,144]

Conclusion

The valorization of nanosized porphyrin-based MOFs and COFs as heterogeneous photosensitizers for singlet oxygen driven antibacterial purposes is currently under intense development aiming at medicinal, sanitisation and agricultural applications. The efficiency of this type II ROS at

eradicating both bacteria and drug resistant bacteria is commendable but combined with type I ROS, the results are impressive. At the molecular level, one of the limitations of nano-MOFs and nano-COFs is the diffusion limit of the ROS when generated inside the materials. For example, with a lifetime of 21 ± 1 μs,[18] the diffusion of $^1O_2(^1\Delta_g)$ from the center of these nanomaterials to the surface appears challenging. Indeed, for a length of action of 60 nm,[51] any distance longer would prove this diffusion outside the nano-object impossible. This issue suggests that the size of these porous nanoparticles should remain within about 100 nm. Moreover, despite the demonstration of a good recyclability (ranging from 5 to 10 cycles), long term application was not demonstrated. This is an important issue since ROS type I are rather very reactive and aging is bound to occur. Despite these two challenges, the current success observed across these recent investigations is based on the rather well-documented precedents on porphyrin- and metalloporphyrin-containing materials and composites, including their use as molecular photosensitizers, and the established knowledge of MOFs' and COFs' preparation, management, and applications. Future developments clearly appear to lie in the design of photo-sanitary textiles and surfaces where toxicity and environmental issues are carefully addressed, perhaps even considering the possibility of recycling. It is noteworthy that all investigations reporting the recyclability of such materials used as photosensitizers or photocatalysts indicated that at least three cycles were performed, which appear insufficient for applications. Applications in agriculture are possible and speak volumes as to the potential versatility of such materials. For now, the cost of production of these nano-photosensitizers remains significant, and the overall cost/benefit ratio must be improved before a serious widespread use can be considered. However based on this review, the urgent outlook lies on the developments of nanocomposites aiming at eradicating the still stubborn drug resistant bacteria, a task that nano-MOFs and nano-COFs tend to do very well through the formation of ROS type I. In addition, the design of antimicrobial textiles and membranes are highly desirable and their production at low cost appears feasible. However, the number of investigations on this topic remains low for the moment indicating clearly that further development is needed. Finally, multiple nano-MOFs, nano-COFs and composites were investigated but the use of different experimental conditions precludes reliable comparison of their efficiencies. Future investigations in this direction are definitely needed.

Declaration of Competing Interest

The authors declare no competing financial interest.

Acknowledgements
This work was supported by the Natural Sciences and Engineering Research Council of Canada, the Fonds de Recherche du Québec-Nature et Technologie and the Centre Quebecois sur les Matériaux Fonctionnels.

References

(1) Herzberg, G. Photography of the Infra-Red Solar Spectrum to Wave-Length 12,900 A. [5]. *Nature*. Nature Publishing Group 1934, p 759. https://doi.org/10.1038/133759a0.
(2) Khan, A. U. The Discovery of the Chemical Evolution of Singlet Oxygen. Some Current Chemical, Photochemical, and Biological Applications. *Int. J. Quantum Chem.* **1991**, *39* (3), 251–267. https://doi.org/10.1002/qua.560390305.
(3) Tian, J.; Huang, B.; Nawaz, M. H.; Zhang, W. Recent Advances of Multi-Dimensional Porphyrin-Based Functional Materials in Photodynamic Therapy. *Coordination Chemistry Reviews*. Elsevier B.V. October 1, 2020, p 213410. https://doi.org/10.1016/j.ccr.2020.213410.
(4) Liu, J.; Huang, J.; Zhang, L.; Lei, J. Multifunctional Metal–Organic Framework Heterostructures for Enhanced Cancer Therapy. *Chem. Soc. Rev.* **2021**, *50* (2), 1188–1218. https://doi.org/10.1039/d0cs00178c.
(5) Jin, L.; Lv, S.; Miao, Y.; Liu, D.; Song, F. Recent Development of Porous Porphyrin-Based Nanomaterials for Photocatalysis. *ChemCatChem* **2021**, *13* (1), 140–152. https://doi.org/10.1002/cctc.202001179.
(6) Zhang, X.; Wasson, M. C.; Shayan, M.; Berdichevsky, E. K.; Ricardo-Noordberg, J.; Singh, Z.; Papazyan, E. K.; Castro, A. J.; Marino, P.; Ajoyan, Z.; Chen, Z.; Islamoglu, T.; Howarth, A. J.; Liu, Y.; Majewski, M. B.; Katz, M. J.; Mondloch, J. E.; Farha, O. K. A Historical Perspective on Porphyrin-Based Metal–Organic Frameworks and Their Applications. *Coordination Chemistry Reviews*. Elsevier B.V. February 15, 2021, p 213615. https://doi.org/10.1016/j.ccr.2020.213615.
(7) Zou, L.; Sa, R.; Lv, H.; Zhong, H.; Wang, R. Recent Advances on Metalloporphyrin-Based Materials for Visible-Light-Driven CO2 Reduction. *ChemSusChem* **2020**, *13* (23), 6124–6140. https://doi.org/10.1002/cssc.202001796.
(8) Feng, L.; Wang, K. Y.; Joseph, E.; Zhou, H. C. Catalytic Porphyrin Framework Compounds. *Trends in Chemistry*. Cell Press June 1, 2020, pp 555–568. https://doi.org/10.1016/j.trechm.2020.01.003.
(9) Nagar, R.; Varrla, E.; Vinayan, B. P. Photocatalysts for Hydrogen Generation and Organic Contaminants Degradation. In *Multifunctional Photocatalytic Materials for Energy*; Elsevier Inc., 2018; pp 215–236. https://doi.org/10.1016/B978-0-08-101977-1.00011-9.
(10) Zhou, Y. B.; Zhan, Z. P. Conjugated Microporous Polymers for Heterogeneous Catalysis. *Chem. - An Asian J.* **2018**, *13* (1), 9–19. https://doi.org/10.1002/asia.201701107.
(11) Zhao, M.; Ou, S.; Wu, C. De. Porous Metal-Organic Frameworks for Heterogeneous Biomimetic Catalysis. *Acc. Chem. Res.* **2014**, *47* (4), 1199–1207. https://doi.org/10.1021/ar400265x.
(12) Hofer, U. The Cost of Antimicrobial Resistance. *Nature Reviews Microbiology*. Nature Publishing Group January 1, 2019, p 3. https://doi.org/10.1038/s41579-018-0125-x.
(13) Mckenna. How to Fight Superbugs: Start Spending Money http://www.wired.com/2015/02/oneill-amr-2/%0AAll Papers/Other/How to Fight Superbugs - Start Spendin... - How_to_Fight_Superbugs_Start_Spending_Money.html (accessed Feb 28, 2021).

(14) Park, J.; Jiang, Q.; Feng, D.; Mao, L.; Zhou, H. C. Size-Controlled Synthesis of Porphyrinic Metal-Organic Framework and Functionalization for Targeted Photodynamic Therapy. *J. Am. Chem. Soc.* **2016**, *138* (10), 3518–3525. https://doi.org/10.1021/jacs.6b00007.
(15) Schweitzer, C.; Schmidt, R. Physical Mechanisms of Generation and Deactivation of Singlet Oxygen. *Chem. Rev.* **2003**, *103* (5), 1685–1757. https://doi.org/10.1021/cr010371d.
(16) Faure, S.; Stern, C.; Guilard, R.; Harvey, P. D. Synthesis and Photophysical Properties of Meso-Substituted Bisporphyrins: Comparative Study of Phosphorescence Quenching for Dioxygen Sensing. *Inorg. Chem.* **2005**, *44* (25), 9232–9241. https://doi.org/10.1021/ic0508573.
(17) Aly, S. M.; Ayed, C.; Stern, C.; Guilard, R.; Abd-El-Aziz, A. S.; Harvey, P. D. Triplet Energy Transfers in Electrostatic Host-Guest Assemblies of Unsaturated Organometallic Cluster Cations and Carboxylate-Containing Porphyrin Pigments. *Inorg. Chem.* **2008**, *47* (21), 9930–9940. https://doi.org/10.1021/ic801006g.
(18) Demel, J.; Kubát, P.; Millange, F.; Marrot, J.; Císařová, I.; Lang, K. Lanthanide-Porphyrin Hybrids: From Layered Structures to Metal-Organic Frameworks with Photophysical Properties. *Inorg. Chem.* **2013**, *52* (5), 2779–2786. https://doi.org/10.1021/ic400182u.
(19) Park, K. C.; Seo, C.; Gupta, G.; Kim, J.; Lee, C. Y. Efficient Energy Transfer (EnT) in Pyrene- and Porphyrin-Based Mixed-Ligand Metal-Organic Frameworks. *ACS Appl. Mater. Interfaces* **2017**, *9* (44), 38670–38677. https://doi.org/10.1021/acsami.7b14135.
(20) Zhao, Y.; Kuang, Y.; Liu, M.; Wang, J.; Pei, R. Synthesis of Metal-Organic Framework Nanosheets with High Relaxation Rate and Singlet Oxygen Yield. *Chem. Mater.* **2018**, *30* (21), 7511–7520. https://doi.org/10.1021/acs.chemmater.8b02467.
(21) Zhang, G. Y.; Cai, C.; Cosnier, S.; Zeng, H. B.; Zhang, X. J.; Shan, D. Zirconium-Metalloporphyrin Frameworks as a Three-in-One Platform Possessing Oxygen Nanocage, Electron Media, and Bonding Site for Electrochemiluminescence Protein Kinase Activity Assay. *Nanoscale* **2016**, *8* (22), 11649–11657. https://doi.org/10.1039/c6nr01206j.
(22) Zhang, G.; Chai, H.; Tian, M.; Zhu, S.; Qu, L.; Zhang, X. Zirconium-Metalloporphyrin Frameworks-Luminol Competitive Electrochemiluminescence for Ratiometric Detection of Polynucleotide Kinase Activity. *Anal. Chem.* **2020**, *92* (10), 7354–7362. https://doi.org/10.1021/acs.analchem.0c01262.
(23) Hideg, É.; Mátai, A.; Bognár, B.; Kálai, T. Chapter 31. EPR Detection (Spin Probes); 2016; pp 121–134. https://doi.org/10.1039/9781782626992-00121.
(24) Keams, D. R.; Khan, A. U.; Duncan, C. K.; Maki, A. H. Detection of the Naphthalene-Photosensitized Generation of Singlet (1δg) Oxygen by Paramagnetic Resonance Spectroscopy. *J. Am. Chem. Soc.* **1969**, *91* (4), 1039–1040. https://doi.org/10.1021/ja01032a050.
(25) Ruzzi, M.; Sartori, E.; Moscatelli, A.; Khudyakov, I. V.; Turro, N. J. Time-Resolved EPR Study of Singlet Oxygen in the Gas Phase. *J. Phys. Chem. A* **2013**, *117* (25), 5232–5240. https://doi.org/10.1021/jp403648d.
(26) Hasegawa, K.; Yamada, K.; Sasase, R.; Miyazaki, R.; Kikuchi, A.; Yagi, M. Direct Measurements of Absolute Concentration and Lifetime of Singlet Oxygen in the Gas Phase by Electron Paramagnetic Resonance. *Chem. Phys. Lett.* **2008**, *457* (4–6), 312–314. https://doi.org/10.1016/j.cplett.2008.04.031.
(27) Rodgers, M. A. J. Singlet Oxygen Quantum Yields; 1987; pp 76–97. https://doi.org/10.1021/bk-1987-0339.ch005.
(28) Hynek, J.; Rathouský, J.; Demel, J.; Lang, K. Design of Porphyrin-Based Conjugated

Microporous Polymers with Enhanced Singlet Oxygen Productivity. *RSC Adv.* **2016**, *6* (50), 44279–44287. https://doi.org/10.1039/c6ra04066g.

(29) Adam, W.; Kazakov, D. V.; Kazakov, V. P. Singlet-Oxygen Chemiluminescence in Peroxide Reactions. *Chemical Reviews*. American Chemical Society September 2005, pp 3371–3387. https://doi.org/10.1021/cr0300035.

(30) Gal, D.; Shuliakovskaya, T.; Vidoczy, T.; Elzemzam, S.; Vasvari, G.; Suemegi, L.; Kuti, Z. <title>Prospects of Radical-Interacting Porphyrin Photosensitizers and Their Possible Use in Photodynamic Therapy</Title>. In *Photodynamic Therapy of Cancer*; Jori, G., Moan, J., Star, W. M., Eds.; SPIE, 1994; Vol. 2078, pp 119–128. https://doi.org/10.1117/12.168684.

(31) Zoltan, T.; Vargas, F.; Rivas, C.; López, V.; Perez, J.; Biasutto, A. Synthesis, Photochemical and Photoinduced Antibacterial Activity Studies of Meso-Tetra(Pyren-1-Yl)Porphyrin and Its Ni, Cu and Zn Complexes. *Sci. Pharm.* **2010**, *78* (4), 767–789. https://doi.org/10.3797/scipharm.1003-13.

(32) Yao, C.; Song, H.; Wan, Y.; Ma, K.; Zheng, C.; Cui, H.; Xin, P.; Ji, X.; Deng, S. Electro-Photodynamic Visualization of Singlet Oxygen Induced by Zinc Porphyrin Modified Microchip in Aqueous Media. *ACS Appl. Mater. Interfaces* **2016**, *8* (50), 34833–34843. https://doi.org/10.1021/acsami.6b10213.

(33) Deng, S.; Zhang, T.; Ji, X.; Wan, Y.; Xin, P.; Shan, D.; Zhang, X. Detection of Zinc Finger Protein (EGR1) Based on Electrogenerated Chemiluminescence from Singlet Oxygen Produced in a Nanoclay-Supported Porphyrin Environment. *Anal. Chem.* **2015**, *87* (18), 9155–9162. https://doi.org/10.1021/acs.analchem.5b01318.

(34) Rossbroich, G.; Garcia, N. A.; Braslavsky, S. E. Thermal-Lensing Measurements of Singlet Molecular Oxygen (1Δg): Quantum Yields of Formation and Lifetimes. *J. Photochem.* **1985**, *31* (1), 37–48. https://doi.org/10.1016/0047-2670(85)85072-3.

(35) Atmaca, G. Y. Measurement of Singlet Oxygen Generation of 9(Hydroxymethyl)Anthracene Substituted Silicon Phthalocyanine by Sono-Photochemical and Photochemical Studies. *J. Mol. Struct.* **2021**, *1226*, 129320. https://doi.org/10.1016/j.molstruc.2020.129320.

(36) Olmsted, J. Photocalorimetric Studies of Singlet Oxygen Reactions. *J. Am. Chem. Soc.* **1980**, *102* (1), 66–71. https://doi.org/10.1021/ja00521a012.

(37) Yuan, J.; Zhou, Q.; Dong, X.; Zhang, B.; Wang, Q.; Yang, Y.; Liao, Y.; Wang, H. Dissolved Oxygen-Assisted Enhancing Room Temperature Phosphorescence of Palladium-Porphyrin in Micelle-Hybridized Supramolecular Gels under UV Irradiation. *Dye. Pigment.* **2019**, *170*, 107654. https://doi.org/10.1016/j.dyepig.2019.107654.

(38) Bonacin, J. A.; Engelmann, F. M.; Severino, D.; Toma, H. E.; Baptista, M. S. Singlet Oxygen Quantum Yields (ΦΔ) in Water Using Beetroot Extract and an Array of LEDs. *J. Braz. Chem. Soc.* **2009**, *20* (1), 31–36. https://doi.org/10.1590/S0103-50532009000100006.

(39) Lutkus, L. V.; Rickenbach, S. S.; McCormick, T. M. Singlet Oxygen Quantum Yields Determined by Oxygen Consumption. *J. Photochem. Photobiol. A Chem.* **2019**, *378*, 131–135. https://doi.org/10.1016/j.jphotochem.2019.04.029.

(40) Mathai, S.; Smith, T. A.; Ghiggino, K. P. Singlet Oxygen Quantum Yields of Potential Porphyrin-Based Photosensitisers for Photodynamic Therapy. *Photochem. Photobiol. Sci.* **2007**, *6* (9), 995–1002. https://doi.org/10.1039/b705853e.

(41) Belfield, K. D.; Bondar, M. V.; Przhonska, O. V. Singlet Oxygen Quantum Yield Determination for a Fluorene-Based Two-Photon Photosensitizer. *J. Fluoresc.* **2006**, *16* (1), 111–117. https://doi.org/10.1007/s10895-005-0001-8.

(42) Wasserman, H. H.; DeSimone, R. W.; Chia, K. R. X.; Banwell, M. G. Singlet Oxygen. In *Encyclopedia of Reagents for Organic Synthesis*; John Wiley & Sons, Ltd: Chichester, UK, 2013; pp 1–11. https://doi.org/10.1002/047084289x.rs035.

(43) Jiang, Z. W.; Zou, Y. C.; Zhao, T. T.; Zhen, S. J.; Li, Y. F.; Huang, C. Z. Controllable Synthesis of Porphyrin-Based 2D Lanthanide Metal–Organic Frameworks with Thickness- and Metal-Node-Dependent Photocatalytic Performance. *Angew. Chemie - Int. Ed.* **2020**, *59* (8), 3300–3306. https://doi.org/10.1002/anie.201913748.

(44) Zhang, L.; Lei, J.; Ma, F.; Ling, P.; Liu, J.; Ju, H. A Porphyrin Photosensitized Metal-Organic Framework for Cancer Cell Apoptosis and Caspase Responsive Theranostics. *Chem. Commun.* **2015**, *51* (54), 10831–10834. https://doi.org/10.1039/c5cc03028e.

(45) Feng, X.; Wang, X.; Wang, H.; Wu, H.; Liu, Z.; Zhou, W.; Lin, Q.; Jiang, J. Elucidating J-Aggregation Effect in Boosting Singlet-Oxygen Evolution Using Zirconium-Porphyrin Frameworks: A Comprehensive Structural, Catalytic, and Spectroscopic Study. *ACS Appl. Mater. Interfaces* **2019**, *11* (48), 45118–45125. https://doi.org/10.1021/acsami.9b17569.

(46) Chen, Y. Z.; Wang, Z. U.; Wang, H.; Lu, J.; Yu, S. H.; Jiang, H. L. Singlet Oxygen-Engaged Selective Photo-Oxidation over Pt Nanocrystals/Porphyrinic MOF: The Roles of Photothermal Effect and Pt Electronic State. *J. Am. Chem. Soc.* **2017**, *139* (5), 2035–2044. https://doi.org/10.1021/jacs.6b12074.

(47) Park, J.; Feng, D.; Yuan, S.; Zhou, H. C. Photochromic Metal-Organic Frameworks: Reversible Control of Singlet Oxygen Generation. *Angew. Chemie - Int. Ed.* **2015**, *54* (2), 430–435. https://doi.org/10.1002/anie.201408862.

(48) He, T.; Ni, B.; Zhang, S.; Gong, Y.; Wang, H.; Gu, L.; Zhuang, J.; Hu, W.; Wang, X. Ultrathin 2D Zirconium Metal–Organic Framework Nanosheets: Preparation and Application in Photocatalysis. *Small* **2018**, *14* (16), 1703929. https://doi.org/10.1002/smll.201703929.

(49) Yang, Y.; Ishida, M.; Yasutake, Y.; Fukatsu, S.; Fukakusa, C.; Morikawa, M. A.; Yamada, T.; Kimizuka, N.; Furuta, H. Hierarchical Hybrid Metal-Organic Frameworks: Tuning the Visible/Near-Infrared Optical Properties by a Combination of Porphyrin and Its Isomer Units. *Inorg. Chem.* **2019**, *58* (7), 4647–4656. https://doi.org/10.1021/acs.inorgchem.9b00251.

(50) Son, H. J.; Jin, S.; Patwardhan, S.; Wezenberg, S. J.; Jeong, N. C.; So, M.; Wilmer, C. E.; Sarjeant, A. A.; Schatz, G. C.; Snurr, R. Q.; Farha, O. K.; Wiederrecht, G. P.; Hupp, J. T. Light-Harvesting and Ultrafast Energy Migration in Porphyrin-Based Metal-Organic Frameworks. *J. Am. Chem. Soc.* **2013**, *135* (2), 862–869. https://doi.org/10.1021/ja310596a.

(51) Patwardhan, S.; Jin, S.; Son, H. J.; Schatz, G. C. Ultrafast Energy Migration in Porphyrin-Based Metal Organic Frameworks (MOFs). *Mater. Res. Soc. Symp. Proc.* **2013**, *1539*, 22–27. https://doi.org/10.1557/opl.2013.987.

(52) Choi, S.; Jung, W. J.; Park, K.; Kim, S. Y.; Baeg, J. O.; Kim, C. H.; Son, H. J.; Pac, C.; Kang, S. O. Rapid Exciton Migration and Amplified Funneling Effects of Multi-Porphyrin Arrays in a Re(I)/Porphyrinic MOF Hybrid for Photocatalytic CO2Reduction. *ACS Appl. Mater. Interfaces* **2021**, *13* (2), 2710–2722. https://doi.org/10.1021/acsami.0c19856.

(53) Förster, T. Zwischenmolekulare Energiewanderung Und Fluoreszenz. *Ann. Phys.* **1948**, *437* (1–2), 55–75. https://doi.org/10.1002/andp.19484370105.

(54) Shaikh, S. M.; Chakraborty, A.; Alatis, J.; Cai, M.; Danilov, E.; Morris, A. J. Light Harvesting and Energy Transfer in a Porphyrin-Based Metal Organic Framework. *Faraday Discuss.* **2019**, *216*, 174–190. https://doi.org/10.1039/c8fd00194d.

(55) Liberman, I.; Shimoni, R.; Ifraemov, R.; Rozenberg, I.; Singh, C.; Hod, I. Active-Site Modulation in an Fe-Porphyrin-Based Metal-Organic Framework through Ligand Axial Coordination: Accelerating Electrocatalysis and Charge-Transport Kinetics. *J. Am. Chem. Soc.* **2020**, *142* (4), 1933–1940. https://doi.org/10.1021/jacs.9b11355.
(56) Ishihara, K. M.; Tian, F. Semiconducting Langmuir-Blodgett Films of Porphyrin Paddle-Wheel Frameworks for Photoelectric Conversion. *Langmuir* **2018**, *34* (51), 15689–15699. https://doi.org/10.1021/acs.langmuir.8b03236.
(57) Ding, G.; Wang, Y.; Zhang, G.; Zhou, K.; Zeng, K.; Li, Z.; Zhou, Y.; Zhang, C.; Chen, X.; Han, S. T. 2D Metal–Organic Framework Nanosheets with Time-Dependent and Multilevel Memristive Switching. *Adv. Funct. Mater.* **2019**, *29* (3), 1806637. https://doi.org/10.1002/adfm.201806637.
(58) Jiang, Y.; Ma, W.; Qiao, Y.; Xue, Y.; Lu, J.; Gao, J.; Liu, N.; Wu, F.; Yu, P.; Jiang, L.; Mao, L. Metal–Organic Framework Membrane Nanopores as Biomimetic Photoresponsive Ion Channels and Photodriven Ion Pumps. *Angew. Chemie* **2020**, *132* (31), 12895–12899. https://doi.org/10.1002/ange.202005084.
(59) Maindan, K.; Li, X.; Yu, J.; Deria, P. Controlling Charge-Transport in Metal-Organic Frameworks: Contribution of Topological and Spin-State Variation on the Iron-Porphyrin Centered Redox Hopping Rate. *J. Phys. Chem. B* **2019**, *123* (41), 8814–8822. https://doi.org/10.1021/acs.jpcb.9b07506.
(60) Kim, M.; Oh, J. S.; Kim, B. H.; Kim, A. Y.; Park, K. C.; Mun, J.; Gupta, G.; Lee, C. Y. Enhanced Photocatalytic Performance of Nanosized Mixed-Ligand Metal-Organic Frameworks through Sequential Energy and Electron Transfer Process. *Inorg. Chem.* **2020**, *59* (17), 12947–12953. https://doi.org/10.1021/acs.inorgchem.0c02079.
(61) Lan, G.; Ni, K.; Veroneau, S. S.; Feng, X.; Nash, G. T.; Luo, T.; Xu, Z.; Lin, W. Titanium-Based Nanoscale Metal-Organic Framework for Type i Photodynamic Therapy. *J. Am. Chem. Soc.* **2019**, *141* (10), 4204–4208. https://doi.org/10.1021/jacs.8b13804.
(62) Keum, Y.; Park, S.; Chen, Y. P.; Park, J. Titanium-Carboxylate Metal-Organic Framework Based on an Unprecedented Ti-Oxo Chain Cluster. *Angew. Chemie - Int. Ed.* **2018**, *57* (45), 14852–14856. https://doi.org/10.1002/anie.201809762.
(63) Xu, X.; Wang, S.; Yue, Y.; Huang, N. Semiconductive Porphyrin-Based Covalent Organic Frameworks for Sensitive Near-Infrared Detection. *ACS Appl. Mater. Interfaces* **2020**, *12* (33), 37427–37434. https://doi.org/10.1021/acsami.0c06022.
(64) Li, H.; Li, H.; Xun, S.; Brédas, J. L. Doping Modulation of the Charge Injection Barrier between a Covalent Organic Framework Monolayer and Graphene. *Chem. Mater.* **2020**, *32* (21), 9228–9237. https://doi.org/10.1021/acs.chemmater.0c02913.
(65) Sobotta, L.; Skupin-Mrugalska, P.; Piskorz, J.; Mielcarek, J. Porphyrinoid Photosensitizers Mediated Photodynamic Inactivation against Bacteria. *European Journal of Medicinal Chemistry*. Elsevier Masson s.r.l. August 1, 2019, pp 72–106. https://doi.org/10.1016/j.ejmech.2019.04.057.
(66) Amos-Tautua, B. M.; Songca, S. P.; Oluwafemi, O. S. Application of Porphyrins in Antibacterial Photodynamic Therapy. *Molecules* **2019**, *24* (13), 2456. https://doi.org/10.3390/molecules24132456.
(67) Day, N. U.; Wamser, C. C.; Walter, M. G. Porphyrin Polymers and Organic Frameworks. *Polym. Int.* **2015**, *64* (7), 833–857. https://doi.org/10.1002/pi.4908.
(68) Gui, B.; Lin, G.; Ding, H.; Gao, C.; Mal, A.; Wang, C. Three-Dimensional Covalent Organic Frameworks: From Topology Design to Applications. *Acc. Chem. Res.* **2020**, *53*

(10), 2225–2234. https://doi.org/10.1021/acs.accounts.0c00357.
(69) De, S.; Devic, T.; Fateeva, A. Porphyrin and Phthalocyanine-Based Metal Organic Frameworks beyond Metal-Carboxylates. *Dalt. Trans.* **2021**, *50* (4), 1166–1188. https://doi.org/10.1039/d0dt03903a.
(70) Huh, S.; Kim, S. J.; Kim, Y. Porphyrinic Metal-Organic Frameworks from Custom-Designed Porphyrins. *CrystEngComm* **2016**, *18* (3), 345–368. https://doi.org/10.1039/c5ce02106e.
(71) Chinchilla, R.; Nájera, C. The Sonogashira Reaction: A Booming Methodology in Synthetic Organic Chemistry. *Chemical Reviews*. American Chemical Society March 2007, pp 874–922. https://doi.org/10.1021/cr050992x.
(72) Miyaura, N.; Suzuki, A. Palladium-Catalyzed Cross-Coupling Reactions of Organoboron Compounds. *Chem. Rev.* **1995**, *95* (7), 2457–2483. https://doi.org/10.1021/cr00039a007.
(73) Chen, X.; Addicoat, M.; Jin, E.; Zhai, L.; Xu, H.; Huang, N.; Guo, Z.; Liu, L.; Irle, S.; Jiang, D. Locking Covalent Organic Frameworks with Hydrogen Bonds: General and Remarkable Effects on Crystalline Structure, Physical Properties, and Photochemical Activity. *J. Am. Chem. Soc.* **2015**, *137* (9), 3241–3247. https://doi.org/10.1021/ja509602c.
(74) Lin, G.; Ding, H.; Chen, R.; Peng, Z.; Wang, B.; Wang, C. 3D Porphyrin-Based Covalent Organic Frameworks. *J. Am. Chem. Soc.* **2017**, *139* (25), 8705–8709. https://doi.org/10.1021/jacs.7b04141.
(75) Jeoung, S.; Kim, S.; Kim, M.; Moon, H. R. Pore Engineering of Metal-Organic Frameworks with Coordinating Functionalities. *Coordination Chemistry Reviews*. Elsevier B.V. October 1, 2020, p 213377. https://doi.org/10.1016/j.ccr.2020.213377.
(76) Zeng, J. Y.; Wang, X. S.; Zhang, M. K.; Li, Z. H.; Gong, D.; Pan, P.; Huang, L.; Cheng, S. X.; Cheng, H.; Zhang, X. Z. Universal Porphyrinic Metal-Organic Framework Coating to Various Nanostructures for Functional Integration. *ACS Appl. Mater. Interfaces* **2017**, *9* (49), 43143–43153. https://doi.org/10.1021/acsami.7b14881.
(77) Begum, S.; Hassan, Z.; Bräse, S.; Wöll, C.; Tsotsalas, M. Metal-Organic Framework-Templated Biomaterials: Recent Progress in Synthesis, Functionalization, and Applications. *Acc. Chem. Res.* **2019**, *52* (6), 1598–1610. https://doi.org/10.1021/acs.accounts.9b00039.
(78) Zhou, W.; Begum, S.; Wang, Z.; Krolla, P.; Wagner, D.; Bräse, S.; Wöll, C.; Tsotsalas, M. High Antimicrobial Activity of Metal-Organic Framework-Templated Porphyrin Polymer Thin Films. *ACS Appl. Mater. Interfaces* **2018**, *10* (2), 1528–1533. https://doi.org/10.1021/acsami.7b14866.
(79) Jiang, L.; Gan, C. R. R.; Gao, J.; Loh, X. J. A Perspective on the Trends and Challenges Facing Porphyrin-Based Anti-Microbial Materials. *Small* **2016**, *12* (27), 3609–3644. https://doi.org/10.1002/smll.201600327.
(80) Deng, Q.; Sun, P.; Zhang, L.; Liu, Z.; Wang, H.; Ren, J.; Qu, X. Porphyrin MOF Dots–Based, Function-Adaptive Nanoplatform for Enhanced Penetration and Photodynamic Eradication of Bacterial Biofilms. *Adv. Funct. Mater.* **2019**, *29* (30), 1903018. https://doi.org/10.1002/adfm.201903018.
(81) Mao, K.; Zhu, Y.; Rong, J.; Qiu, F.; Chen, H.; Xu, J.; Yang, D.; Zhang, T.; Zhong, L. Rugby-Ball like Ag Modified Zirconium Porphyrin Metal–Organic Frameworks Nanohybrid for Antimicrobial Activity: Synergistic Effect for Significantly Enhancing Photoactivation Capacity. *Colloids Surfaces A Physicochem. Eng. Asp.* **2021**, *611*, 125888. https://doi.org/10.1016/j.colsurfa.2020.125888.
(82) Nie, X.; Wu, S.; Huang, F.; Wang, Q.; Wei, Q. Smart Textiles with Self-Disinfection and

Photothermochromic Effects. *ACS Appl. Mater. Interfaces* **2021**, *13* (2), 2245–2255. https://doi.org/10.1021/acsami.0c18474.

(83) Tang, J.; Tang, G.; Niu, J.; Yang, J.; Zhou, Z.; Gao, Y.; Chen, X.; Tian, Y.; Li, Y.; Li, J.; Cao, Y. Preparation of a Porphyrin Metal-Organic Framework with Desirable Photodynamic Antimicrobial Activity for Sustainable Plant Disease Management. *J. Agric. Food Chem.* **2021**, acs.jafc.0c06487. https://doi.org/10.1021/acs.jafc.0c06487.

(84) Nie, X.; Wu, S.; Mensah, A.; Wang, Q.; Huang, F.; Li, D.; Wei, Q. Insight into Light-Driven Antibacterial Cotton Fabrics Decorated by in Situ Growth Strategy. *J. Colloid Interface Sci.* **2020**, *579*, 233–242. https://doi.org/10.1016/j.jcis.2020.06.038.

(85) Hynek, J.; Zelenka, J.; Rathouský, J.; Kubát, P.; Ruml, T.; Demel, J.; Lang, K. Designing Porphyrinic Covalent Organic Frameworks for the Photodynamic Inactivation of Bacteria. *ACS Appl. Mater. Interfaces* **2018**, *10* (10), 8527–8535. https://doi.org/10.1021/acsami.7b19835.

(86) Ding, L. G.; Wang, S.; Yao, B. J.; Li, F.; Li, Y. A.; Zhao, G. Y.; Dong, Y. Bin. Synergistic Antibacterial and Anti-Inflammatory Effects of a Drug-Loaded Self-Standing Porphyrin-COF Membrane for Efficient Skin Wound Healing. *Adv. Healthc. Mater.* **2021**, 2001821. https://doi.org/10.1002/adhm.202001821.

(87) Qiu, H.; Pu, F.; Liu, Z.; Deng, Q. Q.; Sun, P.; Ren, J.; Qu, X. Depriving Bacterial Adhesion-Related Molecule to Inhibit Biofilm Formation Using CeO2-Decorated Metal-Organic Frameworks. *Small* **2019**, *15* (36), e1902522. https://doi.org/10.1002/smll.201902522.

(88) Yu, M.; You, D.; Zhuang, J.; Lin, S.; Dong, L.; Weng, S.; Zhang, B.; Cheng, K.; Weng, W.; Wang, H. Controlled Release of Naringin in Metal-Organic Framework-Loaded Mineralized Collagen Coating to Simultaneously Enhance Osseointegration and Antibacterial Activity. *ACS Appl. Mater. Interfaces* **2017**, *9* (23), 19698–19705. https://doi.org/10.1021/acsami.7b05296.

(89) Ximing, G.; Bin, G.; Yuanlin, W.; Shuanghong, G. Preparation of Spherical Metal–Organic Frameworks Encapsulating Ag Nanoparticles and Study on Its Antibacterial Activity. *Mater. Sci. Eng. C* **2017**, *80*, 698–707. https://doi.org/10.1016/j.msec.2017.07.027.

(90) Luo, Y.; Li, J.; Liu, X.; Tan, L.; Cui, Z.; Feng, X.; Yang, X.; Liang, Y.; Li, Z.; Zhu, S.; Zheng, Y.; Yeung, K. W. K.; Yang, C.; Wang, X.; Wu, S. Dual Metal-Organic Framework Heterointerface. *ACS Cent. Sci.* **2019**, *5* (9), 1591–1601. https://doi.org/10.1021/acscentsci.9b00639.

(91) Han, D.; Han, Y.; Li, J.; Liu, X.; Yeung, K. W. K.; Zheng, Y.; Cui, Z.; Yang, X.; Liang, Y.; Li, Z.; Zhu, S.; Yuan, X.; Feng, X.; Yang, C.; Wu, S. Enhanced Photocatalytic Activity and Photothermal Effects of Cu-Doped Metal-Organic Frameworks for Rapid Treatment of Bacteria-Infected Wounds. *Appl. Catal. B Environ.* **2020**, *261*, 118248. https://doi.org/10.1016/j.apcatb.2019.118248.

(92) Chen, M.; Long, Z.; Dong, R.; Wang, L.; Zhang, J.; Li, S.; Zhao, X.; Hou, X.; Shao, H.; Jiang, X. Titanium Incorporation into Zr-Porphyrinic Metal–Organic Frameworks with Enhanced Antibacterial Activity against Multidrug-Resistant Pathogens. *Small* **2020**, *16* (7), 1906240. https://doi.org/10.1002/smll.201906240.

(93) Sun, Y.; Zhao, C.; Niu, J.; Ren, J.; Qu, X. Colorimetric Band-AIDS for Point-of-Care Sensing and Treating Bacterial Infection. *ACS Cent. Sci.* **2020**, *6* (2), 207–212. https://doi.org/10.1021/acscentsci.9b01104.

(94) Zhang, L.; Cheng, Q.; Li, C.; Zeng, X.; Zhang, X. Z. Near Infrared Light-Triggered Metal

Ion and Photodynamic Therapy Based on AgNPs/Porphyrinic MOFs for Tumors and Pathogens Elimination. *Biomaterials* **2020**, *248*, 120029. https://doi.org/10.1016/j.biomaterials.2020.120029.

(95) Lu, Y.; Zhang, J.; Wei, W.; Ma, D. D.; Wu, X. T.; Zhu, Q. L. Efficient Carbon Dioxide Electroreduction over Ultrathin Covalent Organic Framework Nanolayers with Isolated Cobalt Porphyrin Units. *ACS Appl. Mater. Interfaces* **2020**, *12* (34), 37986–37992. https://doi.org/10.1021/acsami.0c06537.

(96) Pila, T.; Chirawatkul, P.; Piyakeeratikul, P.; Somjit, V.; Sawangphruk, M.; Kongpatpanich, K. Metalloporphyrin-Based Metal–Organic Frameworks on Flexible Carbon Paper for Electrocatalytic Nitrite Oxidation. *Chem. - A Eur. J.* **2020**, *26* (72), 17399–17404. https://doi.org/10.1002/chem.202003206.

(97) Wang, Y.; Zhen, W.; Zeng, Y.; Wan, S.; Guo, H.; Zhang, S.; Zhong, Q. In Situ Self-Assembly of Zirconium Metal-Organic Frameworks onto Ultrathin Carbon Nitride for Enhanced Visible Light-Driven Conversion of CO2 to CO. *J. Mater. Chem. A* **2020**, *8* (12), 6034–6040. https://doi.org/10.1039/c9ta14005k.

(98) Wang, Y. Y.; Chen, S. M.; Haldar, R.; Wöll, C.; Gu, Z. G.; Zhang, J. Van Der Waals Epitaxial Growth of 2D Metal–Porphyrin Framework Derived Thin Films for Dye-Sensitized Solar Cells. *Adv. Mater. Interfaces* **2018**, *5* (21), 1800985. https://doi.org/10.1002/admi.201800985.

(99) Micheroni, D.; Lan, G.; Lin, W. Efficient Electrocatalytic Proton Reduction with Carbon Nanotube-Supported Metal-Organic Frameworks. *J. Am. Chem. Soc.* **2018**, *140* (46), 15591–15595. https://doi.org/10.1021/jacs.8b09521.

(100) Yang, T. H.; Yang, S. H.; Chen, Y. C.; Kurniawan, D.; Chiang, W. H.; Chiu, Y. P.; Kung, C. W. Probing Local Donor-Acceptor Charge Transfer in a Metal-Organic Framework Via a Scanning Tunneling Microscope. *J. Phys. Chem. C* **2020**, *124* (39), 21635–21640. https://doi.org/10.1021/acs.jpcc.0c07477.

(101) Biswas, S.; Chen, Y.; Xie, Y.; Sun, X.; Wang, Y. Ultrasmall Au(0) Inserted Hollow PCN-222 MOF for the High-Sensitive Detection of Estradiol. *Anal. Chem.* **2020**, *92* (6), 4566–4572. https://doi.org/10.1021/acs.analchem.9b05841.

(102) Shi, Z.; Zhang, K.; Zada, S.; Zhang, C.; Meng, X.; Yang, Z.; Dong, H. Upconversion Nanoparticle-Induced Multimode Photodynamic Therapy Based on a Metal-Organic Framework/Titanium Dioxide Nanocomposite. *ACS Appl. Mater. Interfaces* **2020**, *12* (11), 12600–12608. https://doi.org/10.1021/acsami.0c01467.

(103) Tang, J.; Ding, G.; Niu, J.; Zhang, W.; Tang, G.; Liang, Y.; Fan, C.; Dong, H.; Yang, J.; Li, J.; Cao, Y. Preparation and Characterization of Tebuconazole Metal-Organic Framework-Based Microcapsules with Dual-Microbicidal Activity. *Chem. Eng. J.* **2019**, *359*, 225–232. https://doi.org/10.1016/j.cej.2018.11.147.

(104) Ballatore, M. B.; Durantini, J.; Gsponer, N. S.; Suarez, M. B.; Gervaldo, M.; Otero, L.; Spesia, M. B.; Milanesio, M. E.; Durantini, E. N. Photodynamic Inactivation of Bacteria Using Novel Electrogenerated Porphyrin-Fullerene C60 Polymeric Films. *Environ. Sci. Technol.* **2015**, *49* (12), 7456–7463. https://doi.org/10.1021/acs.est.5b01407.

(105) Liu, J.; Yang, Y.; Zhu, W.; Yi, X.; Dong, Z.; Xu, X.; Chen, M.; Yang, K.; Lu, G.; Jiang, L.; Liu, Z. Nanoscale Metal-Organic Frameworks for Combined Photodynamic & Radiation Therapy in Cancer Treatment. *Biomaterials* **2016**, *97*, 1–9. https://doi.org/10.1016/j.biomaterials.2016.04.034.

(106) Chao, Y.; Liang, C.; Yang, Y.; Wang, G.; Maiti, D.; Tian, L.; Wang, F.; Pan, W.; Wu, S.;

Yang, K.; Liu, Z. Highly Effective Radioisotope Cancer Therapy with a Non-Therapeutic Isotope Delivered and Sensitized by Nanoscale Coordination Polymers. *ACS Nano* **2018**, *12* (8), 7519–7528. https://doi.org/10.1021/acsnano.8b02400.

(107) Velásquez-Hernández, M. de J.; Linares-Moreau, M.; Astria, E.; Carraro, F.; Alyami, M. Z.; Khashab, N. M.; Sumby, C. J.; Doonan, C. J.; Falcaro, P. Towards Applications of Bioentities@MOFs in Biomedicine. *Coordination Chemistry Reviews*. Elsevier B.V. February 15, 2021, p 213651. https://doi.org/10.1016/j.ccr.2020.213651.

(108) Mendes, R. F.; Figueira, F.; Leite, J. P.; Gales, L.; Almeida Paz, F. A. Metal-Organic Frameworks: A Future Toolbox for Biomedicine? *Chemical Society Reviews*. Royal Society of Chemistry December 21, 2020, pp 9121–9153. https://doi.org/10.1039/d0cs00883d.

(109) Huang, K.; Li, C.; Li, H.; Ren, G.; Wang, L.; Wang, W.; Meng, X. Photocatalytic Applications of Two-Dimensional Ti3C2MXenes: A Review. *ACS Appl. Nano Mater.* **2020**, *3* (10), 9581–9603. https://doi.org/10.1021/acsanm.0c02481.

(110) Hatz, S.; Lambert, J. D. C.; Ogilby, P. R. Measuring the Lifetime of Singlet Oxygen in a Single Cell: Addressing the Issue of Cell Viability. *Photochem. Photobiol. Sci.* **2007**, *6* (10), 1106–1116. https://doi.org/10.1039/b707313e.

(111) Wan, S.; Gándara, F.; Asano, A.; Furukawa, H.; Saeki, A.; Dey, S. K.; Liao, L.; Ambrogio, M. W.; Botros, Y. Y.; Duan, X.; Seki, S.; Stoddart, J. F.; Yaghi, O. M. Covalent Organic Frameworks with High Charge Carrier Mobility. *Chem. Mater.* **2011**, *23* (18), 4094–4097. https://doi.org/10.1021/cm201140r.

(112) Ballatore, M. B.; Durantini, J.; Gsponer, N. S.; Suarez, M. B.; Gervaldo, M.; Otero, L.; Spesia, M. B.; Milanesio, M. E.; Durantini, E. N. Photodynamic Inactivation of Bacteria Using Novel Electrogenerated Porphyrin-Fullerene C60 Polymeric Films. *Environ. Sci. Technol.* **2015**, *49* (12), 7456–7463. https://doi.org/10.1021/acs.est.5b01407.

(113) Durantini, J.; Otero, L.; Funes, M.; Durantini, E. N.; Fungo, F.; Gervaldo, M. Electrochemical Oxidation-Induced Polymerization of 5,10,15,20-Tetrakis[3- (N-Ethylcarbazoyl)]Porphyrin. Formation and Characterization of a Novel Electroactive Porphyrin Thin Film. *Electrochim. Acta* **2011**, *56* (11), 4126–4134. https://doi.org/10.1016/j.electacta.2011.01.111.

(114) Yamakoshi, Y.; Umezawa, N.; Ryu, A.; Arakane, K.; Miyata, N.; Goda, Y.; Masumizu, T.; Nagano, T. Active Oxygen Species Generated from Photoexcited Fullerene (C 60) as Potential Medicines: O2-. versus 1O2. *J. Am. Chem. Soc.* **2003**, *125* (42), 12803–12809. https://doi.org/10.1021/ja0355574.

(115) Gao, D.; Aly, S. M.; Karsenti, P. L.; Brisard, G.; Harvey, P. D. Ultrafast Energy and Electron Transfers in Structurally Well Addressable BODIPY-Porphyrin-Fullerene Polyads. *Phys. Chem. Chem. Phys.* **2017**, *19* (4), 2926–2939. https://doi.org/10.1039/c6cp08000f.

(116) Gao, D.; Aly, S. M.; Karsenti, P. L.; Brisard, G.; Harvey, P. D. Application of the Boron Center for the Design of a Covalently Bonded Closely Spaced Triad of Porphyrin-Fullerene Mediated by Dipyrromethane. *Dalt. Trans.* **2017**, *46* (19), 6278–6290. https://doi.org/10.1039/c7dt00472a.

(117) Gao, D.; Aly, S. M.; Karsenti, P. L.; Brisard, G.; Harvey, P. D. Increasing the Lifetimes of Charge Separated States in Porphyrin-Fullerene Polyads. *Phys. Chem. Chem. Phys.* **2017**, *19* (35), 24018–24028. https://doi.org/10.1039/c7cp04193d.

(118) Kandambeth, S.; Shinde, D. B.; Panda, M. K.; Lukose, B.; Heine, T.; Banerjee, R. Enhancement of Chemical Stability and Crystallinity in Porphyrin-Containing Covalent Organic Frameworks by Intramolecular Hydrogen Bonds. *Angew. Chemie - Int. Ed.* **2013**,

52 (49), 13052–13056. https://doi.org/10.1002/anie.201306775.
(119) Mosinger, J.; Jirsák, O.; Kubát, P.; Lang, K.; Mosinger, B. Bactericidal Nanofabrics Based on Photoproduction of Singlet Oxygen. *J. Mater. Chem.* **2007**, *17* (2), 164–166. https://doi.org/10.1039/b614617a.
(120) Ringot, C.; Sol, V.; Granet, R.; Krausz, P. Porphyrin-Grafted Cellulose Fabric: New Photobactericidal Material Obtained by "Click-Chemistry" Reaction. *Mater. Lett.* **2009**, *63* (21), 1889–1891. https://doi.org/10.1016/j.matlet.2009.06.009.
(121) Ringot, C.; Saad, N.; Granet, R.; Bressollier, P.; Sol, V.; Krausz, P. Meso-Functionalized Aminoporphyrins as Efficient Agents for Photo-Antibacterial Surfaces. *J. Porphyr. Phthalocyanines* **2010**, *14* (11), 925–931. https://doi.org/10.1142/S1088424610002719.
(122) Kanner, R. C.; Foote, C. S. Singlet Oxygen Emission As a Probe of Excited State Processes in Photooxygenation. In *Oxidative Damage & Repair*; Pergamon, 1991; pp 315–320. https://doi.org/10.1016/b978-0-08-041749-3.50060-7.
(123) Yu, F.; Chen, C.; Yang, G.; Ren, Z.; Cao, H.; Zhang, L.; Zhang, W. An Acid-Triggered Porphyrin-Based Block Copolymer for Enhanced Photodynamic Antibacterial Efficacy. *Sci. China Chem.* **2021**, *64* (3), 459–466. https://doi.org/10.1007/s11426-020-9904-7.
(124) Tian, J.; Zhang, W. Synthesis, Self-Assembly and Applications of Functional Polymers Based on Porphyrins. *Prog. Polym. Sci.* **2019**, *95*, 65–117. https://doi.org/10.1016/j.progpolymsci.2019.05.002.
(125) Ries, A. S.; Cargnelutti, J. F.; Basso, G.; Acunha, T. V.; Iglesias, B. A.; Flores, E. F.; Weiblen, R. Water-Soluble Tetra-Cationic Porphyrins Display Virucidal Activity against Bovine Adenovirus and Bovine Alphaherpesvirus 1. *Photodiagnosis Photodyn. Ther.* **2020**, *31*, 101947. https://doi.org/10.1016/j.pdpdt.2020.101947.
(126) Basso, G.; Cargnelutti, J. F.; Oliveira, A. L.; Acunha, T. V.; Weiblen, R.; Flores, E. F.; Iglesias, B. A. Photodynamic Inactivation of Selected Bovine Viruses by Isomeric Cationic Tetra-Platinated Porphyrins. *J. Porphyr. Phthalocyanines* **2019**, *23* (9), 1041–1046. https://doi.org/10.1142/S1088424619500767.
(127) Tomb, R. M.; Maclean, M.; Herron, P. R.; Hoskisson, P. A.; MacGregor, S. J.; Anderson, J. G. Inactivation of Streptomyces Phage ϕC31 by 405 Nm Light . *Bacteriophage* **2014**, *4* (3), e32129. https://doi.org/10.4161/bact.32129.
(128) Sánchez-Naya, R.; Stepanenko, V.; Mandel, K.; Beuerle, F. Modulation of Crystallinity and Optical Properties in Composite Materials Combining Iron Oxide Nanoparticles and Dye-Containing Covalent Organic Frameworks. *Org. Mater.* **2021**, *03* (01), 017–024. https://doi.org/10.1055/s-0040-1722655.
(129) Ma, H. C.; Zhao, C. C.; Chen, G. J.; Dong, Y. Bin. Photothermal Conversion Triggered Thermal Asymmetric Catalysis within Metal Nanoparticles Loaded Homochiral Covalent Organic Framework. *Nat. Commun.* **2019**, *10* (1), 3368. https://doi.org/10.1038/s41467-019-11355-x.
(130) Singh, C.; Kim, T. W.; Yadav, R. K.; Baeg, J. O. K.; Gole, V.; Singh, A. P. Flexible Covalent Porphyrin Framework Film: An Emerged Platform for Photocatalytic C[Sbnd]H Bond Activation. *Appl. Surf. Sci.* **2021**, *544*, 148938. https://doi.org/10.1016/j.apsusc.2021.148938.
(131) Stratmann, R. E.; Scuseria, G. E.; Frisch, M. J. An Efficient Implementation of Time-Dependent Density-Functional Theory for the Calculation of Excitation Energies of Large Molecules. *J. Chem. Phys.* **1998**, *109* (19), 8218–8224. https://doi.org/10.1063/1.477483.
(132) Ma, B.; Guo, H.; Wang, M.; Wang, Q.; Yang, W.; Wang, Y.; Yang, W. Electrocatalysis and

Simultaneous Determination of Hydroquinone and Acetaminophen Using PN[Sbnd]COF/Graphene Oxide Modified Electrode. *Microchem. J.* **2020**, *155*, 104776. https://doi.org/10.1016/j.microc.2020.104776.

(133) Younis, S. A.; Lim, D. K.; Kim, K. H.; Deep, A. Metalloporphyrinic Metal-Organic Frameworks: Controlled Synthesis for Catalytic Applications in Environmental and Biological Media. *Advances in Colloid and Interface Science*. Elsevier B.V. March 1, 2020, p 102108. https://doi.org/10.1016/j.cis.2020.102108.

(134) Arslanov, V. V; Kalinina, M. A.; Ermakova, E. V; Raitman, O. A.; Gorbunova, Y. G.; Aksyutin, O. E.; Ishkov, A. G.; Grachev, V. A.; Tsivadze, A. Y. Hybrid Materials Based on Graphene Derivatives and Porphyrin Metal-Organic Frameworks. *Russ. Chem. Rev.* **2019**, *88* (8), 775–799. https://doi.org/10.1070/rcr4878.

(135) Li, R.; Xing, L.; Chen, A.; Zhang, X.; Kong, A.; Shan, Y. Covalent Organic Polymer-Derived Carbon Nanotube-Twined Carbon Nanospheres for Efficient Oxygen Electroreduction and Capacitance Storage. *Ionics (Kiel).* **2020**, *26* (2), 927–937. https://doi.org/10.1007/s11581-019-03277-x.

(136) Hou, Y.; Cui, C. X.; Zhang, E.; Wang, J. C.; Li, Y.; Zhang, Y.; Zhang, Y.; Wang, Q.; Jiang, J. A Hybrid of G-C3N4 and Porphyrin-Based Covalent Organic Frameworks: Via Liquid-Assisted Grinding for Enhanced Visible-Light-Driven Photoactivity. *Dalt. Trans.* **2019**, *48* (40), 14989–14995. https://doi.org/10.1039/c9dt03307f.

(137) Zhang, X.; Liu, J.; Qiao, Y.; Kong, A.; Li, R.; Shan, Y. Fe-Boosting Sn-Based Dual-Shell Nanostructures from New Covalent Porphyrin Frameworks as Efficient Electrocatalysts for Oxygen Reduction and Zinc-Air Batteries. *Electrochim. Acta* **2019**, *320*, 134593. https://doi.org/10.1016/j.electacta.2019.134593.

(138) Yao, Y.; Hu, Y.; Hu, H.; Chen, L.; Yu, M.; Gao, M.; Wang, S. Metal-Free Catalysts of Graphitic Carbon Nitride–Covalent Organic Frameworks for Efficient Pollutant Destruction in Water. *J. Colloid Interface Sci.* **2019**, *554*, 376–387. https://doi.org/10.1016/j.jcis.2019.07.002.

(139) Gao, Y.; Lu, J.; Xia, J.; Yu, G. In Situ Synthesis of Defect-Engineered MOFs as a Photoregenerable Catalytic Adsorbent: Understanding the Effect of LML, Adsorption Behavior, and Photoreaction Process. *ACS Appl. Mater. Interfaces* **2020**, *12* (11), 12706–12716. https://doi.org/10.1021/acsami.9b21122.

(140) Gao, Y.; Xia, J.; Liu, D.; Kang, R.; Yu, G.; Deng, S. Synthesis of Mixed-Linker Zr-MOFs for Emerging Contaminant Adsorption and Photodegradation under Visible Light. *Chem. Eng. J.* **2019**, *378*, 122118. https://doi.org/10.1016/j.cej.2019.122118.

(141) Xu, C.; Liu, H.; Li, D.; Su, J. H.; Jiang, H. L. Direct Evidence of Charge Separation in a Metal-Organic Framework: Efficient and Selective Photocatalytic Oxidative Coupling of Amines via Charge and Energy Transfer. *Chem. Sci.* **2018**, *9* (12), 3152–3158. https://doi.org/10.1039/c7sc05296k.

(142) Wang, L.; Jin, P.; Duan, S.; Huang, J.; She, H.; Wang, Q.; An, T. Accelerated Fenton-like Kinetics by Visible-Light-Driven Catalysis over Iron(Iii) Porphyrin Functionalized Zirconium MOF: Effective Promotion on the Degradation of Organic Contaminants. *Environ. Sci. Nano* **2019**, *6* (8), 2652–2661. https://doi.org/10.1039/c9en00460b.

(143) Hao, W.; Chen, D.; Li, Y.; Yang, Z.; Xing, G.; Li, J.; Chen, L. Facile Synthesis of Porphyrin Based Covalent Organic Frameworks via an A2B2 Monomer for Highly Efficient Heterogeneous Catalysis. *Chem. Mater.* **2019**, *31* (19), 8100–8105. https://doi.org/10.1021/acs.chemmater.9b02718.

(144) Wang, L. jie; Wang, R. lei; Zhang, X.; Mu, J. lin; Zhou, Z. yan; Su, Z. min. Improved Photoreduction of CO2 with Water by Tuning the Valence Band of Covalent Organic Frameworks. *ChemSusChem* **2020**, *13* (11), 2973–2980. https://doi.org/10.1002/cssc.202000103.

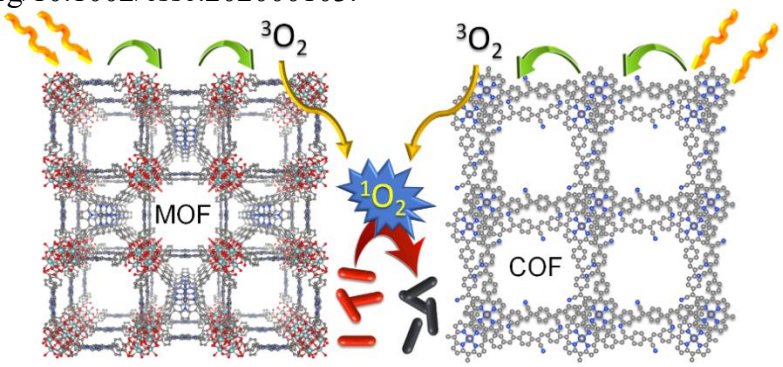

Graphic art